Surface coatings as xenon diffusion barriers on plastic scintillators
– Improving Nuclear-Test-Ban Treaty verification

Lisa Bläckberg

Licentiate Thesis
Department of Physics and Astronomy
2011

UPPSALA
UNIVERSITET

Abstract

This thesis investigates the ability of transparent surface coatings to reduce xenon diffusion into plastic scintillators. The motivation for the work is improved radioxenon monitoring equipment, used with in the framework of the verification regime of the Comprehensive Nuclear-Test-Ban Treaty.

A large part of the equipment used in this context incorporates plastic scintillators which are in direct contact with the radioactive gas to be detected. One problem with such setup is that radioxenon diffuses into the plastic scintillator material during the measurement, resulting in an unwanted memory effect consisting of residual activity left in the detector.

In this work coatings of Al_2O_3 and SiO_2, with thicknesses between 20 and 400 nm have been deposited onto flat plastic scintillator samples, and tested with respect to their Xe diffusion barrier capabilities. All tested coatings were found to reduce the memory effect, and 425 nm of Al_2O_3 showed the most promise.

This coating was deposited onto a complete detector. Compared to uncoated detectors, the coated one presented a memory effect reduction of a factor of 1000.

Simulations and measurements of the expected light collection efficiency of a coated detector were also performed, since it is important that this property is not degraded by the coating. It was shown that a smooth coating, with a similar refractive index as the one of the plastic, should not significantly affect the light collection and resolution. The resolution of the complete coated detector was also measured, showing a resolution comparable to uncoated detectors.

The work conducted in this thesis proved that this coating approach is a viable solution to the memory effect problem, given that the results are reproducible, and that the quality of the coating is maintained over time.

List of Papers

This thesis is based on the following papers, which are referred to in the text by their roman numbers.

Paper I.
   Investigations of surface coatings to reduce memory effect in plastic scintillator detectors used for radioxenon detection

L. Bläckberg, A. Fay, I. Jõgi, S. Biegalski, M. Boman, K. Elmgren, T. Fritioff, A. Johansson, L. Mårtensson, F. Nielsen, A. Ringbom, M. Rooth, H. Sjöstrand, M. Klintenberg
   Nuclear Instruments and Methods in Physics Research A 645 (2011) 84-91

My contribution: I performed the absolute memory effect measurements and analysis, and wrote the major part of the paper.

Paper II.
   Effects of surface coatings on the light collection in plastic scintillators used for radioxenon detection

L. Bläckberg, M. Klintenberg, A. Ringbom, H. Sjöstrand
   Submitted to Physica Scripta, as part of the proceedings of the Nordic Conference of Nuclear Physics, Stockholm, june 13-17 2011

My contribution: I did the simulations, experiments and analysis. I wrote the paper.

Paper III.
   Measurements of memory effect and resolution for an Al_2O_3 coated plastic scintillator used for radioxenon detection

L. Bläckberg, T. Fritioff, M. Klintenberg, L. Mårtensson, F. Nielsen, A. Ringbom, H. Sjöstrand
   Manuscript

My contribution: I did the major part of the experimental work and analysis. I wrote the paper.

Contents

iv

List of Abbreviations

AFM	Atomic Force Microscopy
ALD	Atomic Layer Deposition
ARIX	Automatic Radioanalyzer for Isotopic Xenon
ARSA	Automated Radioxenon Sampler-Analyzer
ATM	Atmospheric Transport Modeling
CAMAC	Computer Automated Measurement And Control
CE	Conversion Electron
CEA	Commisariat à l'Énergie Atomique
CTBT	Comprehensive nuclear-Test-Ban Treaty
CTBTO	Comprehensive nuclear-Test-Ban Treaty Organization
FOI	Totalförsvarets Forskningsinstitut
FWHM	Full Width Half Maximun
GCI	Global Communication Infrastructure
HEU	High Enriched Uranium
IAEA	International Atomic Energy Agency
IDC	International Data Center
IMS	International Monitoring System
INGE	International Noble Gas Experiment
KRI	Khoplin Radium Institute
MCNP	Monte Carlo N-Particle transport code
MDC	Minimum Detectable Concentration
MIPF	Medical Isotope Production Facility
NDC	National Data Center
NIM	Nuclear Instrumentation Module
NNWS	Non Nuclear Weapon States
NPP	Nuclear Power Plant
NPT	Non-Proliferation Treaty
NWS	Nuclear Weapon States
OSI	On Site Inspection
PECVD	Plasma Enhanced Chemical Vapor Deposition
PM-tube	PhotoMultiplier-tube
PNNL	Pacific Northwest National Laboratory
PTBT	Partial Test Ban Treaty
ROI	Region Of Interest
SAUNA	Swedish Automatic Unit for Noble gas Acquisition
SPALAX	Système de Prélèvement Automatique en Ligne avec l'Analyse du Xénon
TMA	TriMethylAluminum
YAP	Yttrium Aluminum Perovskite

Chapter 1

Introduction

The aim of this work is to reduce unwanted diffusion of noble gases into plastic scintillator materials. The motivation is to improve the monitoring of radioactive xenon in the atmosphere, so that clandestine nuclear test explosions can be discovered. Such monitoring is performed continuously within the verification regime of the Comprehensive Nuclear-Test-Ban Treaty (CTBT) [1].

A large part of the equipment used for this purpose incorporates plastic scintillators, which are in direct contact with the radioactive gas to be detected. One major drawback with such detector setup is that xenon easily diffuses into the porous plastic material [2]. The result is a residual activity left in the detector during following measurements, leading to an elevated system detection limit [3]. This residual activity is here referred to as the "Memory Effect".

The low activity expected to reach a monitoring system from a nuclear explosion, in combination with the sometimes high xenon background from nuclear power plants and medical isotope production facilities [4, 5], makes the memory effect an issue that is important to solve.

This work focuses on one particular detection system, the SAUNA system which is developed by the Swedish Defence Research Agency [6]. SAUNA detects radioxenon by means of a beta-gamma coincidence spectrometer, where a cylindrical plastic scintillator cell acts as a container for the xenon sample during the measurements. Beta particles and conversion electrons (CE) are detected by this plastic scintillator, and coincident gammas and X-rays by a surrounding NaI(Tl) crystal.

Various solutions to the memory effect have been proposed, including exchange of the plastic scintillator for an inorganic scintillator, like scintillating glass or YAP [7], or saturation of the plastic material with stable xenon. The approach that was chosen for further studies was to coat the existing detector with a film acting as a gas diffusion barrier. The advantage of this technique is that it requires a minimal modification of the existing systems, and the analysis of the data they produce. The only thing that needs to be exchanged is the actual plastic scintillator cell. This approach has previously been tested with various non-transparent metal coatings [7]. A theoretical study of graphene as also been performed, showing that even a defect graphene sheet would work as a sufficiently good barrier for this application [8].

In this thesis two transparent coating materials have been investigated; Al_2O_3 and SiO_2, deposited using Atomic Layer Deposition (ALD) and Plasma

Enhanced Chemical Vapor Deposition (PECVD), respectively. These materials have been deposited onto plastic scintillator samples, as well as a complete detector, and tested with respect to their ability of stopping xenon from diffusing into the plastic scintillator material.

Apart from being a good Xe diffusion barrier, it is also important that the coating does not impair the detector resolution. Both simulations and measurements have been performed in order address this issue, and predict how the light collection and resolution is affected by a coating.

The project has been a collaboration between Uppsala University, the Swedish Defence Research Agency (FOI), and the University of Texas at Austin, USA.

The thesis is divided into 6 chapters, where Chapter 2 gives some background information regarding nuclear disarmament and the verification regime of the CTBT. Chapter 3 describes relevant theory regarding radioxenon detection, the memory effect, and surface coatings as gas diffusion barriers. Chapter 4 describes simulations and measurements conducted in order to evaluate the effect of a coating on the detector resolution. Chapter 5 contains a description of measurements of xenon diffusion in coated and uncoated flat plastic scintillator samples, as well as a complete Al_2O_3 coated detector. Finally, Chapter 6 contains some final conclusions, and an outlook for the future.

Chapter 2

Background - Nuclear disarmament

In august 1945, during the final stages of the second world war, the United States dropped 2 nuclear fission bombs over Japan. The uranium bomb "*Little boy*" exploded over Hiroshima on august 6th, and 3 days later the plutonium bomb "*Fat man*" was dropped over Nagasaki. The use of the nuclear bombs resulted in the death of 210 000 people directly at the time of the explosions, and 130 000 more within 5 years after the events [9].

After these events the work of preventing more countries to acquire the extremely powerful nuclear weapons begun. At the same time work was conducted to spread knowledge and technology for peaceful nuclear energy. The technology and physics basis is similar for the two applications, which has lead to a need for strict control over nuclear materials and technologies, to assure that they are used for the right purpose.

In 1957 the International Atomic Energy Agency (IAEA) was formed, with the purpose of promoting research and development of nuclear technology for peaceful uses, as well as to establish and develop safety standards [10]. IAEA was later given the responsibility of applying safeguards for verification of compliance with the Nuclear-Non-Proliferation Treaty (NPT) [11]. NPT is one of the international treaties formed to prevent the proliferation of nuclear weapons. This chapter will describe the NPT (Section 2.1), and the Comprehensive Nuclear-Test-Ban Treaty (CTBT) in Section 2.2. The CTBT bans all nuclear explosions, and is the treaty leading to the need of the work conducted in this thesis.

2.1   The Nuclear Non-Proliferation Treaty

In 1968 the Nuclear Non-Proliferation Treaty (NPT) was opened for signature, and the treaty entried into force 2 years later [12]. Before 1968 USA, Russia (as the Soviet Union), United Kingdom, France and China possessed nuclear weapons. These countries were recognized by the NPT as the five Nuclear Weapons States (NWS) [1]. The NWS are obliged by the treaty not to transfer nuclear weapons to Non-Nuclear Weapons States (NNWS), or in any way assist these countries in acquiring nuclear weapons [13]. The NNWS are obliged not to manufacture or receive any nuclear weapons. The NPT thus resulted in that

many countries abandoned their nuclear weapons programs.

The NPT also encourages the charing of equipment and knowledge of nuclear technology for peaceful uses. The NPT does not however, contain a clear obligation of nuclear disarmament for the NWS, but states that work should be conducted towards total nuclear disarmament. In addition to the five recognized NWS, three additional countries have developed and tested nuclear weapons after 1968; India, Pakistan, and the Democratic Peoples Republic of Korea (DPRK). India and Pakistan never signed the NPT, and DPRK was a member state but withdrew its membership in 2003. The only other country in the world standing outside the treaty is Israel, who are believed to possess nuclear weapons, but this has never been confirmed.

2.2 CTBT and nuclear testing

One shortcoming of the NPT is its lack of disarmament obligations for the NWS. In order to address this the Comprehensive Nuclear-Test-Ban Treaty (CTBT) was opened for signature in 1996. The CTBT bans all nuclear explosions in all environments, and it has up until today been signed by 182 states and ratified by 155 [1].

The treaty has not yet entried into force. It will do so 6 months after all 44 so called Annex 2 states have both signed and ratified the treaty. The Annex 2 states are those that in 1996 were on IAEA's list of countries with nuclear research or nuclear reactors. The states missing for entry into force are DPRK, India and Pakistan who have neither signed nor ratified, and USA, China, Iran, Israel, Egypt and Indonesia who have signed the treaty but not ratified it.

The CTBT is a continuation of the Partial Test Ban Treaty (PTBT), which bans all nuclear test explosions except those underground. The motivation for the PTBT was to slow down the nuclear arms race and to stop the nuclear fallout into the atmosphere [1].

Between 1945 and 1996, more than 2000 nuclear tests were performed by the 5 NWS, and one test each by India and Pakistan. Before 1963, when the PTBT entried into force, most of the explosions were atmospheric, however after 1963 most tests have been conducted underground. Since the CTBT opened for signature in 1996 only 5 tests have been conducted; one by India in 1998, two by Pakistan the same year, and two by DPRK in 2006 and 2009.

2.2.1 Verification regime

When the CTBT entries into force there is a need for a verification regime in order to verify its compliance. Right now such regime is being constructed by the Comprehensive Nuclear-Test-Ban Treaty Organization (CTBTO) [1]. The verification regime consists of an International Monitoring System (IMS), which, when it is completed, will consist of 321 monitoring stations, supported by 16 radionuclide labs, spread over the world as shown in Figure 2.1.

The IMS is designed to detect energy release and radionuclide production, which are two basic phenomena caused by a nuclear explosion. The energy release is monitored using seismic, infrasound, and hydroacoustic measurement systems.
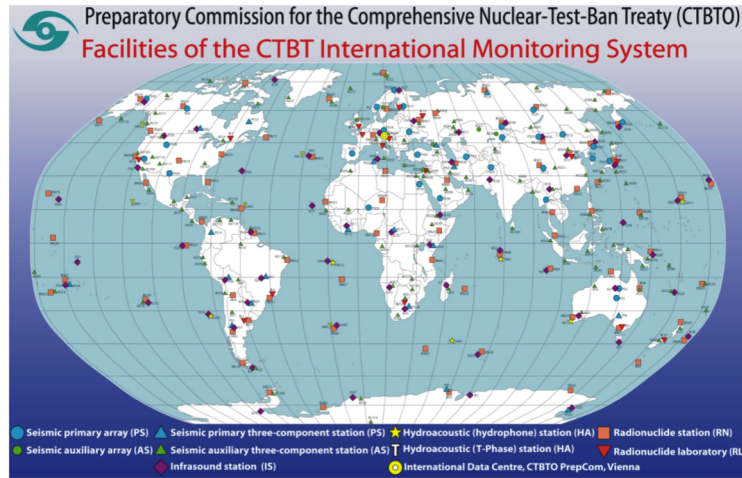
Figure 2.1: The International Monitoring System [1].

In order to distinguish a nuclear explosion from a conventional one, it is necessary to detect radionuclides released in the explosion. This is done using aerosol stations detecting airborne radioactive particles, and noble gas detection systems monitoring radioxenon in the atmosphere.

To find the location and source term of an explosion, backtracking of the radioactive plume can be performed using Atmospheric Transport Modeling (ATM). To be able to detect an explosion anywhere on earth many of the IMS stations are located in remote inaccessible areas. As of november 2011 almost 80% of the network is up and running.

The IMS could also be used for other purposes, such as tsunami alerts, or radioactivity measurement after a nuclear accident. This was proven during, and after, the Tohuku earthquake and tsunami, and the following accident in the Fukushima power plant in 2011. The energy release from the earthquake and radionuclides released from the power plant were detected, both in Japan and in the rest of the world. The radionuclide stations allowed to follow the plume of radioactivity released from Fukushima as it spread over the entire northern hemisphere, both in the form of radioactive particles and as noble gases. It was also clear from this experience that the IMS is not designed to detect such high activities as those present in the vicinity of the Fukushima power plant.

Data from all the monitoring stations are continuously being sent via a Global Communication Infrastructure (GCI), to the International Data Center (IDC) located in Vienna, Austria, where it is processed and analyzed. Data is also available to National Data Centres (NDC) in the member states, who are able to perform independent analysis of the data. The Swedish Defence Research Agency (FOI) are responsible for the Swedish NDC, and also operates two IMS stations. One is a seismic station located in Hagfors, and the other one is a radionuclide station in Kista consisting of both a particulate and a noble gas detection system [14].

When the treaty entries into force, CTBTO will also be able to perform On Site Inspections (OSI) when a violation of the treaty is suspected, and the technology to aid such inspections is now being developed [1].

2.2.2 Monitoring equipment

The monitoring equipment used in the IMS are divided into 4 modalities; seismic, hydroacoustic, infrasound, and radionuclide measurement stations. The first three modalities are based on waveform analysis, dedicated to detect the energy release from the explosion, taking place underground, underwater, or in the atmosphere. The complementing radionuclide modality is needed to verify the nuclear nature of an explosion [1].

Seismic monitoring

The seismic network consist of 170 measurement stations where seismic sensors monitor waves propagating through earth [1]. The waves can originate from for example explosions or earthquakes. The purpose of the seismic monitoring is to discover underground nuclear explosions. One advantage of seismic waves is that they travel very fast, an an event can be measured anywhere on earth with in 10 minutes after occurring. There are both fast traveling body waves inside the earth, and slower and more destructive surface waves. There are two types of seismic monitoring stations used in the IMS, seismic arrays and three-component sensors. Seismic arrays consist of various sensors spread over a wide area, and three component sensors only contain one sensor and therefore have a larger error, but are more cost-effective.

Hydroacoustic monitoring

Hydroacoustic monitoring stations measure acoustic energy traveling in water. Since water very efficiently transport such energy, it is enough with 11 stations to cover all oceans on earth [1]. Hydroacoustic signals can be used to discover nuclear tests underwater, but also atmospheric and underground tests performed near the ocean surface or near the coast, respectively.

There are two kinds of stations in the IMS measuring hydroacoustic waves. The first type are seismic three-component sensors located on small islands with steep slopes. They measure the acoustic wave as it is transformed into a seismic one upon hitting land. The other type of systems are underwater hydrophones. These consist of microphones located at a depth between 600 and 1200 meters. From the microphones there are cables transferring the signal to an island, which can be located as far as 100 km from the microphones.

Infrasound monitoring

The third wave-sensing modality in the IMS is infrasound monitoring. Infrasound is acoustic waves with very low frequency, not audible for the human ear [1]. Infrasound can be generated both by natural sources like volcanoes, earthquakes, and storms, and by man made sources like explosions and rocket launching. The infrasonic waves are detected by sensors measuring micropressure changes in the atmosphere. There are 60 infrasound stations in the IMS,

which can be used to detect atmospheric tests as well as shallow underground explosions.

Radionuclide monitoring

The final modality is radionuclide monitoring. This modality is needed to verify if an event picked up by the other 3 monitoring systems, is nuclear in nature or not. The idea of the radionuclide network is to capture and measure the radioactive debris which is released in the explosion, and spread in the atmosphere by winds. The radioactivity can either be solid fission products attached to dust particles, or radioactive noble gases. There are 80 stations monitoring the radioactive particles [1]. This is done by sampling air and passing it through a filter which captures a large part of the particles. This filter is exchanged every day, and the radioisotopes it contains are identified through gamma ray spectroscopy.

40 of the 80 radionuclide stations are to be equipped with additional radioxenon monitoring systems. These systems samples air, extracts a xenon sample, and measures its activity. Four different radioxenon detection systems have been developed specifically for use in the IMS, within the framework of the International Noble Gas Experiment (INGE) [15]. The INGE collaboration was formed in order to facilitate the development of equipment meeting the specific requirements of use in the IMS. The IMS systems need to be able to detect extremely low concentrations of airborn radioxenon, work automatically 24 hours a day without the need of continuous maintenance, and have a time resolution of no more than 24 hours. The developed systems are: the Automatic Radioanalyzer for Isotopic Xenon (ARIX) [16], the Automated Radioxenon Sampler-Analyzer (ARSA) [17], the Swedish Automatic Unit for Noble Gas Acquisition (SAUNA) [6], and the Système de Prélèvement Automatique en Ligne avec l'Analyse du Xénon (SPALAX) [18]. ARIX is developed by Khoplin Radium Institute (KRI), Russia, ARSA by the Pacific Northwest National Laboratory (PNNL), USA, SAUNA by the Swedish Defence Research Agency (FOI), Sweden, and SPALAX by Commisariat à l'Énergie Atomique (CEA), France.

As a support for the radionuclide network, there are 16 radionuclide laboratories. These allow for reanalysis of suspicious samples, as well as routine controls of the performance of the stations.

The remainder of this thesis will focus on equipment used for radioxenon monitoring.

Chapter 3

Theory

This chapter contains theory relevant for the work conducted in this thesis. In Sections 3.1 to 3.4 the reasons for monitoring radioxenon are explained, as well as how it is detected in the IMS. Section 3.5 discusses radiation detection in general, and scintillator detectors in particular. The radioxenon detection in the SAUNA system is described in Section 3.6, and the memory effect in Section 3.7. Finally the approach of using a surface coating as a xenon diffusion barrier is discussed in Section 3.8.

3.1   Why detect radioxenon?

In the event of a nuclear explosion a variety of fission products are created. In an underground explosion the majority of these will remain in the cavity formed by the explosion, and can thus not be detected by the IMS. However, around 15% of the fission products come in the form of noble gases, which due to their inert chemical properties can reach the surface and allow for detection. Even in the event of a well contained explosion noble gases can travel through fractures and faults in the soil, and be pumped to the surface with the aid of barometric changes [19]. The detection of such gases can thus be crucial in order to identify an explosion as nuclear.

One noble gas that is created in large amounts in a nuclear explosion is xenon, since its mass is found close to the maximum of the fission mass yield curve for both uranium and plutonium [20]. Around 20 different isotopes of xenon are created in the event of a nuclear explosion, of which four have half lives that are suitable for detection by the IMS. These are ^{131m}Xe ($t_{1/2}$=11.9 days), ^{133m}Xe ($t_{1/2}$=2.2 days), ^{133}Xe ($t_{1/2}$=5.2 days), and ^{135}Xe ($t_{1/2}$=9.1 h).

Half lives of the order of days are preferable since it is long enough for the isotopes to travel large distances in the air before decaying, so that they can reach an IMS measurement facility. It is also short enough so that xenon releases from for example nuclear power plants decays relatively rapidly, and the normal xenon background is kept at moderate levels [21].
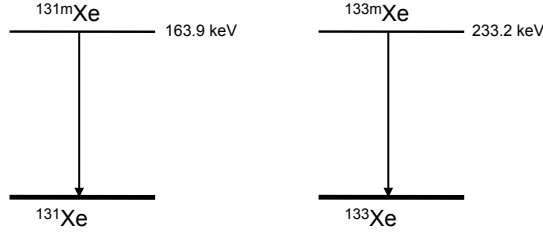
Figure 3.1: Decay schemes for ^{131m}Xe and ^{133m}Xe. The decay to the ground state takes place either through the emission of a gamma photon, or a conversion electron in combination with Xe X-rays.

3.2 Radioxenon decay

As mentioned in Section 3.1 there are 4 radioxenon isotopes that are of interest for detection by the IMS. These are ^{131m}Xe, ^{133m}Xe, ^{133}Xe, and ^{135}Xe, and in this section their respective decays are explained. In Table 3.1 the energies and yields of the dominant decays from each of the 4 isotopes are listed.

^{131m}Xe and ^{133m}Xe

^{131m}Xe and ^{133m}Xe are isomers of ^{131}Xe and ^{133}Xe, respectively. An isomer is a long lived excited state of a nucleus, sometimes also called a metastable state [20]. The isomer decays to the ground state nucleus through isomeric transition, where a gamma ray carrying the excitation energy is emitted.

Competing with the emission of a gamma ray is internal conversion, where a conversion electron (CE) in combination with X-rays are emitted. In this process the nucleus transfers its excitation energy to an electron in one of the lower shells, which can then escape, and the atom is left ionized. The kinetic energy of the emitted conversion electron correspond to the difference between the excitation energy and the binding energy of the electron. The energy of all CEs emitted from a certain shell, in internal conversion from a certain excited state, is thus the same. The emission of the CE creates a vacancy in the shell where it used to be bound. This vacancy is almost instantaneously filled with an electron from an outer shell, resulting in the emission of characteristic X-rays carrying the difference in binding energy between the different shells.

Figure 3.1 shows the decay schemes of the two radioxenon isomers. The transition indicated by the arrow can, as explained, either take place through the emission of a gamma ray carrying the full excitation energy, or internal conversion. For both ^{131m}Xe and ^{133m}Xe the decay to the ground state is dominated by internal conversion. The most dominating CEs are the ones originating from the K-shell, resulting conversion electrons with energies of 129 keV from ^{131m}Xe, and 199 keV from ^{133m}Xe. The branching ratios for these decays are 61 and 63.5% respectively.

For both isomers the CEs are emitted together with Xe X-rays at around 30 keV. The ground state of ^{131}Xe is stable, but the one of ^{133}Xe is not, and its decay is described in the following paragraph.

Table 3.1: The dominant decays from the radioxenon isotopes of interest for detection by the IMS [22].

Isotope	Half life	Radiation	Energy (keV)	Intensity (%)
^{131m}Xe	11.930 d			
		gamma	163.93	1.98
		CE	129.37	61.0
		X-ray	29.46	15.4
		X-ray	29.78	28.5
		X-ray	33.63	8.3
		X-ray	34.50	1.95
^{133m}Xe	2.198 d			
		gamma	233.22	10.16
		CE	198.66	63.5
		X-ray	29.46	16.0
		X-ray	29.78	29.7
		X-ray	33.63	8.61
		X-ray	34.50	2.03
^{133}Xe	5.2474 d			
		beta	346.4 (endpoint)	99.12
		gamma	79.61	0.28
		gamma	80.99	37.0
		CE	45.01	52.9
		X-ray	30.63	13.54
		X-ray	30.97	25.0
		X-ray	34.99	7.31
		X-ray	35.91	1.78
^{135}Xe	9.14 h			
		beta	910 (endpoint)	96
		gamma	249.77	90
		gamma	608.15	2.9
		CE	214	5.7
		X-ray	30.63	1.49
		X-ray	30.97	2.75
		X-ray	34.99	0.49
		X-ray	35.91	0.18

Both ^{133}Xe and ^{135}Xe decay through β^- emission. The effect of a β^- decay on the nucleus, is that one neutron is converted to a proton. In order to conserve the total electric charge a negatively charged beta particle is also created [20]. The beta particle is identical to an electron, and it will be immediately ejected from the nucleus. The energy difference Q between the initial and final nuclear states, is shared between the beta particle and an antineutrino also emitted in the decay. The energy of the emitted beta particle thus ranges from zero up to an endpoint energy defined by Q. As opposed to conversion electrons which have discrete energies, the beta spectrum is continuous between 0 and Q.

The daughter nucleus contains one less neutron, but an additional proton, compared to its parent. The decay has thus resulted in the formation of a new element.

Figure 3.2(a) shows the decay scheme of ^{133}Xe. The daughter nucleus of ^{133}Xe is ^{133}Cs, which is stable. There are various possible beta decays, but the dominating one has an endpoint energy of 346.4 keV, taking place in 99.12% of the decays (indicated by ①) in the figure). This dominating decay leaves the nucleus at a 80.99 keV excited state of ^{133}Cs. The transition ② to the ground state of ^{133}Cs takes place either by emission of an 80.99 keV gamma, or internal conversion with the emission of a CE in association with Cs X-rays. The dominating CE has an energy of 45 keV and originates from the K-shell. The beta and gamma decay has a total branching ratio of 37%, and the total branching ratio of the beta, CE and X-ray decay is 53%.

^{135}Xe has ^{135}Cs as daughter nucleus, and its decay scheme is shown in Figure 3.2(b). The decay is dominated by a β^- with an endpoint energy of 910 keV ③, leaving the daughter nucleus at a 249.8 keV excited state.

The transition ④ to the ground state takes place either through emission of a 249.8 keV gamma, or internal conversion. For this isotope it is the gamma emission that is dominating, having a total branching ratio of 90%. The daughter nucleus, ^{135}Cs, is in this case also radioactive, with a long half life of 2.3×10^6 years.

3.3   Beta-Gamma coincidence spectroscopy

One problem with simultaneously measuring the decay of all four previously described isotopes, is that they have overlapping spectra in both the electron and photon domain (see Table 3.1). All four isotopes has X-ray emissions in the 30 keV region. Although they have separate gamma lines, it can be difficult to distinguish for example the 164 keV gamma peak from ^{131m}Xe from the ambient background, due to its very low intensity. This fact makes the use of beta-gamma coincidence spectroscopy a convenient choice for measuring the activity of each isotope [17, 23, 6].

When it comes to internal conversion, the X-rays are emitted very rapidly after the CE. Furthermore, the lifetimes of the excited states of ^{133}Cs, and ^{135}Cs are of the order of nanoseconds. The result is that the beta decay, and the following gamma or CE + X-ray are be emitted almost instantaneously.

A beta-gamma coincidence spectrometer generally incorporates multiple detectors, where electrons are detected in one detector, and photons in the other.
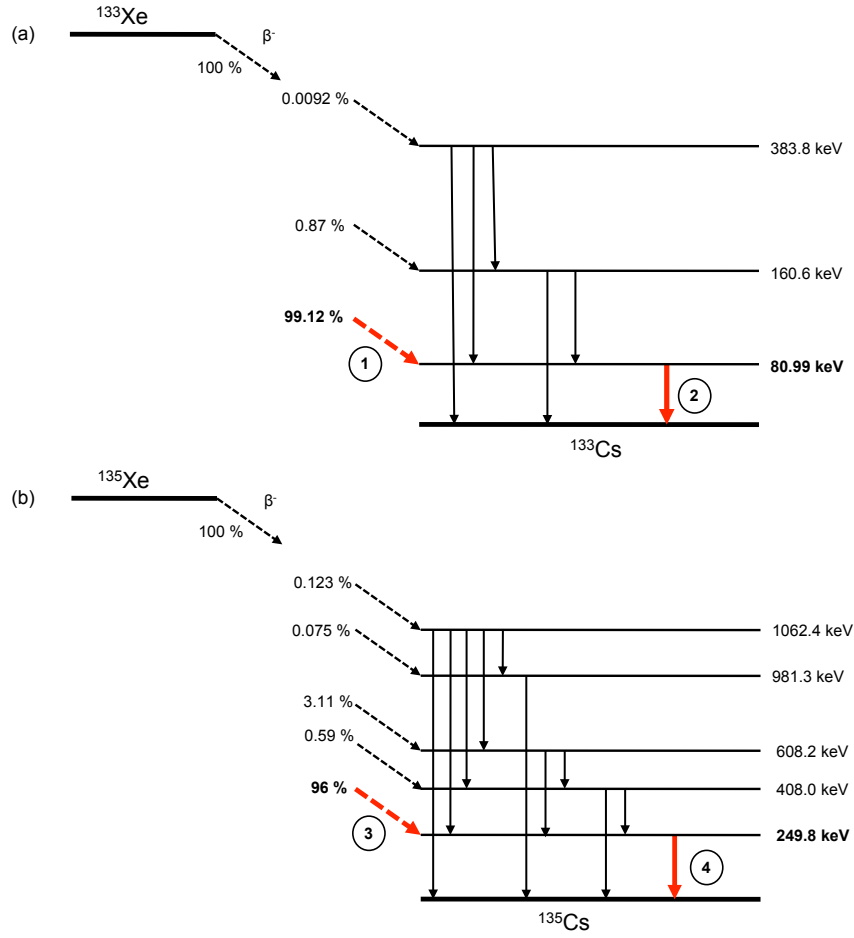
Figure 3.2: Decay scheme for ^{133}Xe (a), and ^{135}Xe (b). The dashed arrows correspond to β^- decay, and the solid ones are gamma transitions which in some cases can be substituted by internal conversion. The red bold arrows correspond to the strongest transitions for each of the isotopes.

An event is recorded if an interaction has been detected in both detectors within a short interval defined by a coincidence window. The coincidence window states the time interval within which two events are considered to originate from the same decay.

The result of the measurement is a two-dimensional (2D) spectrum where each event is characterized by both a photon energy and an electron energy. An added advantage of the coincidence technique is that the influence of ambient background activity is drastically reduced, since all events without a coincident complementary radiation are removed.

Figure 3.3 shows a schematic picture of a 2D coincidence spectrum containing all four xenon isotopes. On the x-axis is the beta (or CE) energy of the event, and on the y-axis is the gamma (or X-ray) energy. The different regions in the figure corresponds to the dominating decays of each isotope:

^{131m}**Xe (green):** A 129 keV CE in coincidence with a Xe X-ray of around 30 keV.

^{133m}**Xe (blue):** A 199 keV CE in coincidence with a Xe X-ray of around 30 keV.

^{133}**Xe (yellow):** The decay from this isotope is seen in two different regions, both originating from a beta decay with endpoint energy of 346 keV. The beta decay can either be followed by a 81 keV gamma emission, or a 45 keV CE together with a 30 keV X-ray, as explained in Section 3.2. The upper region shows the beta distribution in coincidence with the 81 keV gamma ray, and the lower region shows the same beta distribution in coincidence with the CE and a 30 keV X-ray. The lower region is shifted in beta energy since the 45 keV from the CE is added to the beta energy in each event.

^{135}**Xe (red):** The dominating beta decay with endpoint energy of 910 keV is detected in coincidence with a 250 keV gamma ray.

3.3.1 Determination of atmospheric concentrations

From a measured 2D-spectrum, with the characteristics of the one shown in Figure 3.3, the activities of each of the xenon isotopes can be determined, and from these their atmospheric concentrations. For the Swedish IMS system SAUNA, the analysis of the spectra is based on the so called Net Count Calculation method [24, 25]. This method is based on 10 regions of interest (ROIs), defining interesting parts of the spectrum, as shown in Figure 3.4.

Sometimes the sample can contain radon contamination, which contributes to the background in the measured spectrum, through the decay of its daughters ^{214}Bi and ^{214}Pb. ROI 1 contains counts from ^{214}Pb, and is used to correct for the radon contamination. The other ROIs can be compared to Figure 3.3, and are used to determine the activity of each of the four xenon isotopes. ROI 2 contains counts from ^{135}Xe, and ROI 3 counts from ^{133}Xe. ROI 4 contains counts from both ^{133}Xe, ^{131m}Xe, and ^{133m}Xe, and therefore ROI 5-10 are used to determine the number of counts related to each of these three isotopes.
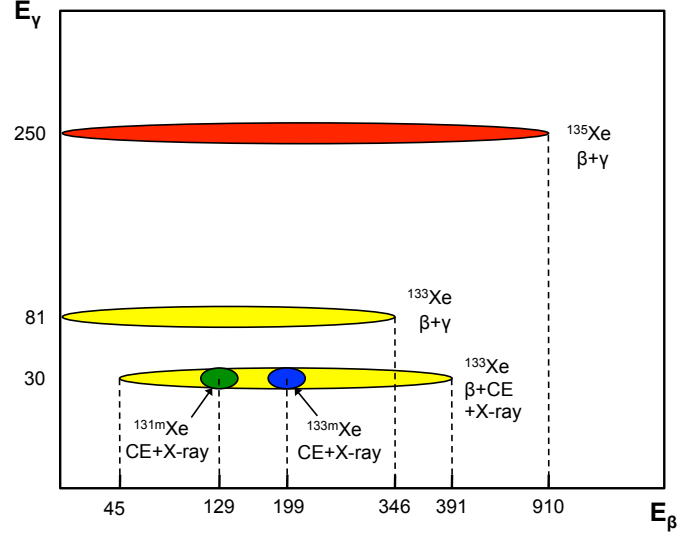
14

Figure 3.3: Schematic picture of a 2D beta-gamma coincidence spectrum containing ^{135}Xe (red), ^{133}Xe (yellow), ^{131m}Xe (green), and ^{133m}Xe (blue). All energies are given in keV. A real spectrum containing ^{133}Xe can be seen in Figure 5.7
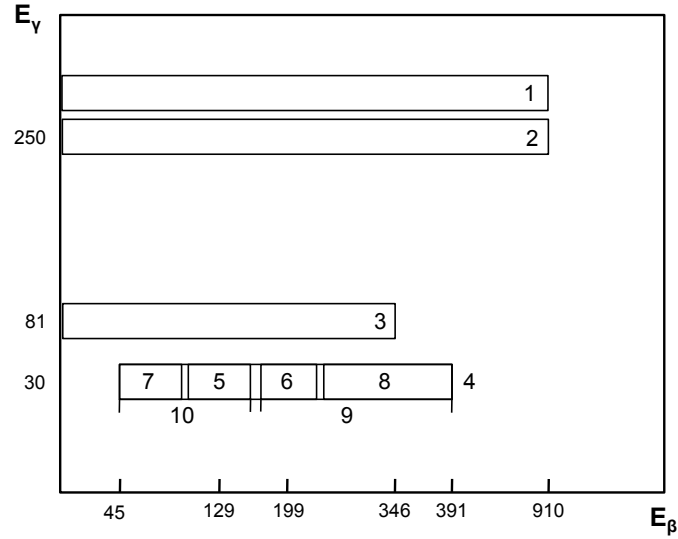

Figure 3.4: Regions of interest used in the analysis of radioxenon beta-gamma spectra.

For each isotope i the net number of counts c_i corresponding to a certain decay can be determined by correcting for interferences from other isotopes as well as background.

From the net number of counts the atmospheric concentration C_i of each of the isotopes at the start sample collection, can be determined according to [24]:

$$C_i = \frac{c_i}{\varepsilon_{\beta\gamma}\beta\gamma}\frac{\lambda^2}{F_C F_P F_A}\frac{t_{coll}}{V},$$ (3.1)

where the different parameters correspond to:

c_i = The net number of counts from a certain decay of isotope i.

$\varepsilon_{\beta\gamma}$ = The absolute detection efficiency in the ROI containing the decay of interest.

$\beta\gamma$ = The branching ratio of the decay.

λ = The decay constant of isotope i.

$F_C = 1 - e^{-\lambda t_{coll}}$, is a factor correcting for decay of the sample activity during the collection time t_{coll} of the air volume.

$F_P = e^{-\lambda t_{proc}}$, is a factor correcting for decay of the sample activity during the processing time t_{proc} of the xenon sample.

$F_A = 1 - e^{-\lambda t_{meas}}$, is a factor correcting for decay of the sample activity during the measurement time t_{meas} of the sample activity.

t_{coll} = The collection time of the air sample.

V = The sampled air volume. V is found by dividing the volume of the xenon sample with the known concentration of stable xenon in air. The volume of the xenon sample is determined in the gas chromatograph in the processing unit of the system, and the radioactive xenon only constitute a very small fraction of the total xenon sample.

The main contributions to the uncertainty in a calculated concentration, are the uncertainties in the net number of counts c, and in the air volume V [6].

3.4   Source discrimination

Nuclear explosions are unfortunately not the only source of radioxenon in the atmosphere, a fact that makes the task of identifying an event as nuclear rather complicated. The mere detection of atmospheric radioxenon is thus not enough to conclude that a nuclear explosion has taken place. The absolute activities of the different isotopes are not of much help either, since the gases are often very diluted before reaching an IMS station. This has lead to the use of isotopic ratios to distinguish an explosion from a civilian source [26].

The main contributors to the global radioxenon background are nuclear power plants (NPPs), and medical isotope production facilities (MIPFs) [5, 4]. Common for NPPs, MIPFs, and nuclear explosions is that in all cases xenon

Table 3.2: Xenon yields and isotopic ratios from thermal fission of ^{235}U [4].

	Independent yield (%)	Cumulative yield (%)
^{131m}Xe	3.48E-07	4.05E-02
^{133m}Xe	1.89E-03	1.89E-01
^{133}Xe	6.66E-04	6.70E+00
^{135}Xe	7.85E-02	6.54E+00
^{133m}Xe/^{131m}Xe	5.43E+03	4.67E+00
^{135}Xe/^{133}Xe	1.18E+02	9.76E-01

is produced as by-product in neutron induced fission. The main difference between the three cases is the neutron irradiation time of the target. In uranium or plutonium nuclear bombs this irradiation is almost instantaneous. The most common reaction in MIPFs is neutron irradiation of a high enriched uranium (HEU) target with the aim to produce ^{99}Mo. In this case the irradiation time is on the order of days. The longest irradiation times are found in NPPs where the irradiation time of the nuclear fuel is of the order of months or years. The different irradiation times is something that has been found to have great impact on the ratios between the different xenon isotopes [5, 4].

3.4.1 Nuclear explosions

In a nuclear explosion, radioxenon can be produced both as a direct fission product in the explosion, or through decay from parent nuclei also created in the explosion [21]. Because of this one usually speaks about two different fission yields of a certain isotope; the independent yield and the cumulative yield. The independent yield of an isotope is the number of nuclei created instantaneously, expressed per fission taking place. The cumulative yield is the number of nuclei that will ever exist as a result of the fission. Here the decay of all parent nuclei are taken into account.

Table 3.2 lists the expected yields from all four isotopes in the case of thermal fission of ^{235}U. Listed are also the expected isotopic ratios in the two cases which, as can be seen, differs by an order of magnitude for both listed ratios.

The ratios measured by the IMS will thus depend on when the noble gases were separated from their parents. In the case of full fractionation at the time of the explosion only the independent yield will be observed. If on the other hand the noble gases are contained in the cavity created by an underground explosion, together with their parents for hours or days before being vented, the ingrowth from parent nuclei will be significant. It is thus important to take into account both cases when differentiating nuclear explosions from civilian sources. A result from this behavior is that information on the leaking process from an underground explosion, can be drawn from the measured ratios. The different half lives of the four isotopes also causes the ratios to change over time as the radioxenon decays. The result of this is that the ratios can also provide information on the timing of the event.

3.4.2 Nuclear power plants

For NPPs the radioxenon isotopic ratios reaches equilibrium values after a couple of weeks of full power operation. During reactor shutdown and startup these ratios can however change quite drastically, and it is thus not enough to only consider the equilibrium value for source discrimination [5].

In Ref. [5] simulations of both expected reactor ratios in light water reactors, and explosion ratios were performed, resulting in an approach that can be used to differentiate between NPPs and a nuclear explosion. This approach is illustrated in Figure 3.5. Two isotopic ratios have been plotted against each other in a log-log plot, where the isotope with the longer half life is in the denominator on each axis. The red dashed line separates the ratios in a reactor domain to the left of the line, and an explosion domain to the right. The slope of the separation line is determined by the decay constants of the four isotopes, so that the explosion ratios always end up in the explosion domain, independent of when they are measured. Theoretically, all radioxenon created in the fuel matrix in a nuclear reactor should end up to the left of the line, except during the first 20-30 days of irradiation of fresh fuel. The expected ratios during these first days unfortunately overlap with the ones expected from a nuclear explosion.

The slope of the discrimination line is determined from the decay constants of the four isotopes. The result is that the line will always be on the left side of the explosion ratios even though these change in time. The blue line in the figure represents the ratios from a nuclear explosion, where the dashed line shows the behavior over time after full fractionation at the time of the explosion, and the solid line when ingrowth from parent nuclei takes place. The dot represents the time of the explosion, and both ratios decrease with time since the longer lived isotope is in the denominator in both cases.

In this figure all four isotopes are used, but it is also possible to do similar graphs with less than four isotopes, if not all are measured. Such graphs does however not provide as efficient screening as if all four isotopes are measured. This screening approach has been validated with measured radioxenon concentrations, as well as reported annual releases from NPPs [27].

3.4.3 Medical isotope production facilities

Medical isotope production facilities have proven to be the major source of radioxenon in the atmosphere, even though there are much fewer MIPFs than NPPs on earth [4]. One problem with MIPFs is that the irradiation times of the HEU target is only of the order of days, resulting in isotopic ratios very similar to the ones expected from a nuclear explosion. The ratios expected in a release from a MIPF are affected mostly by the irradiation times, and the delay lines of the gas before being released into the atmosphere.

Suggestions to solve this issue are that the MIPFs prolong their irradiation times and implement processes that reduce the xenon emissions. It would also be very useful to measure the emissions of xenon in the stack, and use this information together with atmospheric transport modeling in the analysis of IMS data.
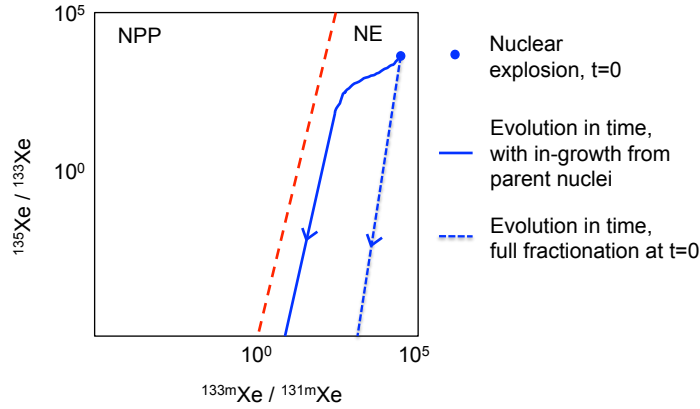
Figure 3.5: Schematic picture illustrating the source discrimination approach proposed by Kalinowski et. al., involving multiple isotopic ratios [5]. The red dashed discrimination line divides the plot in a nuclear power plant domain (left), and a nuclear explosion domain (right). The blue dot represent the time of the explosion, and the lines the evolution in time of the expected ratios. The solid line is when in-growth from parent nuclides takes place, and the dashed one when the radioxenon gas is separated from the other fission products at the time of the explosion.

3.4.4 The DPRK test in 2006

On october 9th in 2006, the Democratic Peoples Republic of Korea (DPRK) announced that they had performed a nuclear test, and the event was also detected by the seismic network in the IMS. At that time the closest noble gas systems in operation were located in Ulaanbaatar (Mongolia), Spitsbergen (Norway), Stockholm (Sweden), and Yellowknife (Canada). Due to the winds at the time the only place where radioxenon from the explosion was detected was in Yellowknife, 7000 km away from the explosion site [28]. ^{133}Xe was seen in elevated concentrations around 2 weeks after the explosion, but none of the other isotopes. The elevated activity concentration could however not be explained by any other source in the vicinity of the noble gas system. Atmospheric transport modeling also showed the xenon signal to be consistent with a release from explosion site in DPRK at the time of the event.

A mobile SAUNA xenon sampler, [29], was also sent to South Korea, and used to collect to xenon samples close to the DPRK border. The samples were then transported to FOI in Sweden for analysis [30]. Samples were collected on october 11-14, and analyzed on october 14-21. The measurements showed measurable concentrations of ^{133}Xe and ^{133m}Xe consistent with a nuclear explosion.

The above mentioned measurements all contained xenon concentrations of the order of mBq/m^3, a fact stressing the importance of very low detection limits of the IMS noble gas systems. The importance of knowledge of the radioxenon background, as well as potential radioxenon sources, in combination with atmospheric transport modeling were also proven to be crucial in order to identify the explosion as nuclear.

19

3.5 Radiation detectors

To detect radiation such as the photons and electrons emitted in the decay of radioxenon, some type of interaction with a detector material is needed. Electrons are charged particles and will continuously interact with other electrons in the material through the Coulomb force. These interactions causes them to lose energy and deviate from their initial path. The lost energy results in ionization and excitation of the atoms and molecules in the detector material [31].

Photons are not charged, and does not lose their energy continuously in the material like electrons. Instead they are absorbed or scattered in single events, where part, or all, of their energy is transferred to electrons (or nuclei) within the detector medium. These secondary electrons will then deposit their energy continuously in the material through coulomb interactions.

There are three main processes responsible for loss of photon energy in a material:

Compton scattering: Is an elastic collision between the photon and an electron in the material. The photon will scatter and transfer some of its energy to the electron. Compton scattering is less probable to occur for higher photon energies.

Photoelectric absorption: Results in total absorption of the photon by an electron initially bound to an atom. This electron is ejected with an energy corresponding to the difference between the energy of the incident photon, and the electron binding energy. The probability of photoelectric absorption also decreases with increasing photon energy

Pair production: If the energy of the incoming photon is above 1.02 MeV pair production can occur. Here the photon is completely absorbed and its energy is converted into a an electron-positron pair.

In many cases the same photon undergoes various of the described processes before all its energy is lost. The preferred interaction is the photoelectric absorption, since the full photon energy is deposited in one single event.

There are many different types of radiation detectors, for example semiconductor detectors and ionization chambers [31]. Another common detector type are scintillators, which are described in the following section.

3.5.1 Scintillators

Scintillators are characterized by their ability to reemit the absorbed energy in the form of light, a process called fluorescence. The emitted light is transmitted through the detector medium and reflected at surfaces, until it reaches some kind of photosensor that can convert the light to an electrical signal. Sometimes the coupling between the photosensor and the scintillator is aided by transparent light guides [31].

Common light converters are photomultiplier tubes (PM-tubes), where the scintillator light ejects photoelectrons from a photocathode, and the signal is amplified in a dynode chain. Ideally the output is proportional to the amount of incoming light. PM-tubes are generally most efficient for light in the visible range.

A good scintillator should have a high scintillation efficiency (i. e. light yield), and be transparent to the wavelengths of its own emission [32]. It is also important that a good optical match to the PM-tube is achieved [31].

Scintillators are generally divided into two groups, depending on their material compositions; organic and inorganic scintillators. In both cases the emission of scintillation light takes place by de-excitation through transitions in the electronic structure in the detector material. All non-radiative processes, that compete with the fluorescence, such as conversion of the excitation energy to heat, results in a lower light yield from the scintillator. This quenching can be caused by for example impurities.

Organic scintillators

In organic scintillators light is emitted in transitions between levels in the electronic structure of organic molecules. Organic scintillators are mainly composed of carbon and hydrogen, and thus have a low effective atomic number Z, which results in low probability for all three previously described interactions between photons and a detector material. Therefore it is not common to use organic scintillators for photon detection. They are however widely used for detection of other types of radiation (alpha, beta, other charged particles, and neutrons).

Organic scintillators can either be pure organic crystals, or the scintillating molecules can be solved in a liquid or plastic. Plastic scintillators are widely used since they are easy to manufacture in different shapes and sizes [31].

In the case of liquid and plastic scintillators, the conversion of radiation energy to scintillator light is a three step process (for pure crystals the second step is omitted).

First the energy of the incident radiation is absorbed, mainly by the solvent molecules since they constitute the major fraction of the material. Secondly the excitation energy migrates to the scintillator molecules, which de-excite and emit photons in the third step. The energy of the emitted photons is determined by the difference in energy between the excited and ground states of the molecules. The organic molecules are chosen such that this energy corresponds to visible light.

Sometimes an additional constituent is added to the solution, acting as a wavelength shifter. These molecules absorb the scintillator light and re-emit it at a different wavelength. This can be useful to match the light with the highest sensitivity of the PM-tubes.

Inorganic scintillators

The effect of radiation incident on an inorganic crystal, is that electrons are elevated from the valence band to the conduction band. The result are so called electron-hole pairs, consisting of an extra electron in the conduction band, and a vacancy in the valence band. The de-excitation, and emission of scintillator photons, occurs when these electron-hole pairs recombine.

Inorganic scintillators can either be self activated, or they can be doped. In self activated scintillators the recombination takes place by the electron jumping from the bottom of the conduction band to the top of the valence band, and the energy of the emitted photon will correspond to the band gap of the crystal.
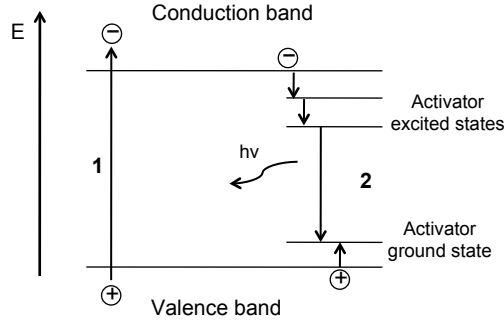
Figure 3.6: Schematic picture of the scintillation process in an activated inorganic crystal. In step 1 an electron is excited to the conduction band, leaving a hole in the valence band. In step 2 the electron-hole pair migrates to an activator site, where the hole ionizes the activator. The electron then recombines with the hole with the emission of a photon. The energy of the photon is characterized by the energy levels of the activator, and is lower than the full band gap of the crystal.

In doped (activated) scintillators impurities are introduced into the host crystal. These impurities can have energy levels within the bandgap of the crystal, offering an alternative way for de-excitation with the emission of photons with an energy level lower than the full band gap of the crystal (see Figure 3.6). The composition of the crystal and the choice of activators can be tailored such that the emitted photons are in the visible range.

3.5.2   Detector resolution

The resolution is an important property of a radiation detector. It determines the ability of the detector to distinguish between particles of different energies. In many detectors, for example scintillators, the resolution reflects the spread in the pulse height generated by the detector as response to a particle of certain type and energy [31].

In a radiation detector, the particle energy is transformed into charge carriers, where the number of charge carriers (i.e. amount of charge Q) produced is related to the particle energy. In the case of scintillators this is a two-step process, where the particle energy is first transformed to light, which in turn is converted to electrons at the photocathode of the PM-tube. In this case it is the photoelectrons that are the charge carriers. To process the signal from the detector, it is generally coupled to a preamplifier, where a capacitor is loaded with the charge Q and subsequently discharges. The maximum voltage over the capacitor during this process is ideally proportional to the charge Q, and thus also the energy of the detected particle. The output from the preamplifier is a series of pulses, with pulse heights reflecting the energy of each detected particle. The pulses are normally collected in a histogram according to their pulse heights.

Ideally, the response to identical particles would always be the same, and the spectrum generated by a monoenergetic source would be a sharp spike. Such
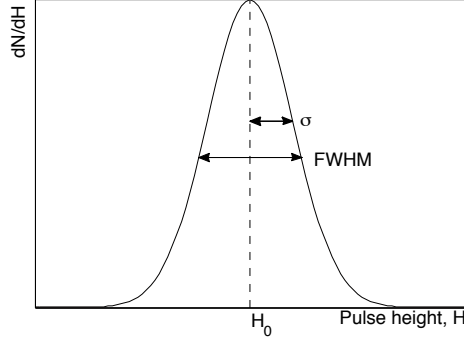
Figure 3.7: Pulse heigh spectrum illustrating the definition of the FWHM.

ideal situation is unfortunately not possible to achieve. The reason for this is that all detectors present some degree of statistical fluctuations in the number of charge carriers produced for a specific particle energy. These fluctuations can be assumed to follow poisson statistics, so the number of charge carriers created in response to a certain particle energy varies around the mean number N, with a standard deviation given by $\sigma = \sqrt{N}$. The resulting peak in the pulse height spectrum thus have a width corresponding to $\sigma = \sqrt{N}$, if the only contribution to the peak broadening are the statistical fluctuations in the number of charge carriers. There are generally also other sources of fluctuations such as drifts in the operating parameters and electronic noise, which result in additional peak broadening.

The final resolution R of the detector, for a certain energy is defined as:

$$R = \frac{FWHM}{H_0} \qquad (3.2)$$

where H_0 is the average pulse height and $FWHM$ is the Full Width Half Maximum, which is defined as the width of the peak at the level defined by half the peak maximum, see Figure 3.7. If the peak shape is gaussian $FWHM = 2\sqrt{2ln2}\sigma \approx 2.35\sigma$ is valid.

If there are various contributions to the broadening of the peak, and if these are symmetrical and independent, the shape of the peak tend to be gaussian with a $FWHM_{total}$ defined by:

$$FWHM_{total}^2 = FWHM_1^2 + FWHM_2^2 + FWHM_3^2... \qquad (3.3)$$

where $FWHM_i$ correspond to the contribution i.

Resolution in scintillator detector systems

Scintillators are detectors that have relatively poor resolution, and therefore broad peaks compared to high resolution detectors. In most cases the dominant contributions to peak broadening in scintillators are:

23

- Statistical fluctuations in the number of photoelectrons created at the photocathode per event.

- Variations in response over the active volume of the detector. These variations are usually dominated by non-uniform light collection efficiency.

- Electronic noise in the components used in the detector system.

- Drifts in operating parameters during the course of the measurement. For scintillator detector systems these drifts are usually related to the PM-tubes.

The dominating contribution is generally the photoelectron statistics. The spatial variations in detector response can also be a significant contribution for large detectors, or detectors with complex shape. Both these contributions are governed by the collection of the scintillator light created in the detector. The light collection efficiency is defined as the fraction of all created photons that reaches the photocathodes and are converted to electrons. A high light collection efficiency results in a large number of photoelectrons created per event. The statistical variance in the number of created photoelectrons is, according to poisson statistics, given by $\sigma = \sqrt{N}$, and the relative variance thus decreases with an increased number of photoelectrons N. In addition to a high light collection efficiency, it is also important that it is uniform over the active volume of the detector. A spread in the number of photons reaching the PM-tube depending on where in the detector the interaction took place, will also add to the peak broadening.

A less than perfect light collection can be due to self absorption in the scintillator material, or losses at the surfaces of the material. Self absorption can be due to overlapping absorption and emission spectra, impurities in the material or inherent absorption in the solvent (in the case of organic scintillators) [33]. These losses are however usually only significant for large scintillators.

Since light is emitted in all angles in a scintillation event, part of the created light will inevitably undergo surface interactions before reaching the PM-tubes. When light hits a surface it can either be reflected back into the material, or it can be transmitted into the adjacent medium. If the incident angle is larger than a certain critical angle, total internal reflection occurs. If the incident angle is smaller than the critical angle part of the light is reflected, and part is transmitted into the adjacent medium, according to Fresnels formulae [31]. The critical angle θ_c is determined from Snell's law of refraction to:

$$\theta_c = \sin^{-1} \frac{n_2}{n_1}, \tag{3.4}$$

where n_1 and n_2 are the refractive indices of the scintillator and the adjacent medium, respectively. In order to increase the light collection efficiency an external reflector is often used to recapture some of the transmitted light. The reflector can be either specular or diffuse, but it has been shown that often a diffuse reflector is to prefer, since these spread the light in arbitrary angles, and the risk of the light being trapped by multiple internal reflections is smaller. There are various different external reflectors used, like white paint, aluminum foil, and teflon tape.

One surface where total internal reflection is not desirable is the interface between the scintillator and the photocathode of the PM-tube. The photocathode often has a glass window with a refractive index similar to those of many scintillators. Even if this is the case, it is important that there is no gap between the two materials since this will increase the risk of light being reflected back into the scintillator. To avoid this problem optical grease, and/or optical pillows with refractive indices close to the one of the scintillator are often used, in order to assure that there is no air between the scintillator and the PM-tube.

It should also be noted that an increased number of surface reflection increases the mean path travelled by the photons, which will make self absorption more significant.

3.6 Radioxenon detection using the SAUNA system

Almost half of the radioxenon detection systems used within the IMS are SAUNA systems. The prototype SAUNA was developed by the Swedish Defence Research Agency (FOI) [6]. The system was commercialized in 2004, and the current version, SAUNA II, is manufactured by the company Gammadata SAUNA Systems [29].

The system consists of three main parts, performing sampling, processing and activity measurement of a xenon sample. In the sampling and processing units a xenon sample of typically 1.3 cm^3 is extracted from around 15 m^3 of air. The xenon sample is then introduced into a detector where the activities of ^{131m}Xe, ^{133m}Xe, ^{133}Xe, and ^{135}Xe are measured during 11 hours.

The detector is a beta-gamma coincidence spectrometer consisting of a 6.2 cm^3 cylindrical plastic scintillator cell, inserted into a drilled hole in a NaI(Tl) crystal, as illustrated in Figure 3.8. The plastic scintillator cell also acts as a container for the xenon sample during the measurement.

Electrons are less penetrating than photons, so the beta particles and conversion electrons are detected by the plastic scintillator cell, and the gammas and X-rays by the NaI(Tl) crystal. The thickness of the walls of the plastic scintillator cell is 1 mm, chosen so that the 346 keV electrons from the β^- decay of ^{133}Xe are fully stopped.

The NaI(Tl) is read out by one PM-tube, and the plastic scintillator cell by two (one at each end). An event is recorded in the 2D histogram if a signal is measured in all three PM-tubes in coincidence. The detector design is based on the one used in the american ARSA system [17].

The system contains 2 identical detector units working in parallel where one detector measures the gas background in the empty detector while the other one measures a sample, and vice versa. The gas background measurement is needed to correct for residual activity left in the detector from previous samples. This residual activity is here referred to as the memory effect, which is described further in Section 3.7.
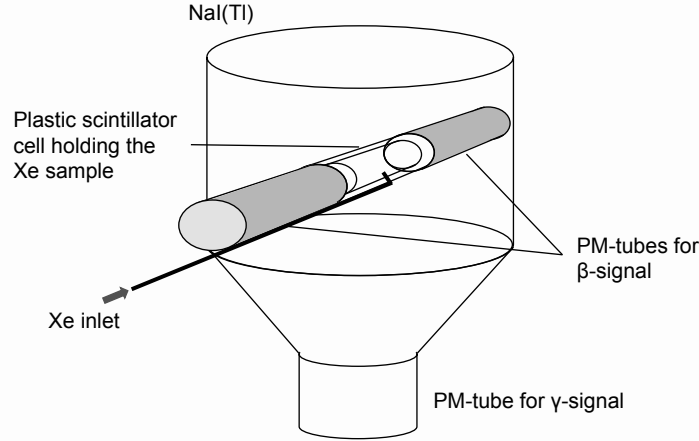
Figure 3.8: The SAUNA detector. The xenon sample is located inside the plastic scintillator cell during the measurement. The Signal from the NaI(Tl) crystal is read out by one PM-tube, and the signal from the plastic scintillator by two PM-tubes.

3.7 The memory effect

One problem with the current design of the SAUNA system is that part of the xenon sample diffuses into the plastic scintillator material of the beta cell during the measurements [2]. This is also a problem for the ARSA and the ARIX systems, which also contains beta gamma coincidence spectrometers involving plastic scintillators [34, 35].

Today this memory effect is compensated for by measuring a gas background measurement of the evacuated cell, prior to each sample measurement. The residual activity in the gas background measurement can then be subtracted from the sample activity. For this reason, the SAUNA system contains two detectors working in parallel to allow for continuous monitoring. This approach is however not ideal, and leads to an elevation of the system detection limit.

Figure 3.9 shows the count rate of ^{133}Xe in the ROI at 81 keV gamma energy and 0-346 keV beta energy (ROI 3 in Figure 3.4), in a series of sample measurements, and gas background measurements. The data is taken from an IMS SAUNA system installed in Charlottesville, VA, USA. The shown count rate is the net count rate, where background counts and interferences from other isotopes have been subtracted from the total measured number of counts in the ROI. It is from this figure clearly seen that a high count rate in a sample measurement is followed by an elevated count rate also in the following gas background measurement. It is also seen that a strong sample leaves traces of residual activity in the gas background various measurements ahead.

In Figure 3.10 part of the data in Figure 3.9 has been used to plot the ^{133}Xe count rate in the gas background measurements as a function of the count rate in the previous sample measurement. Only the data where the sample count rate
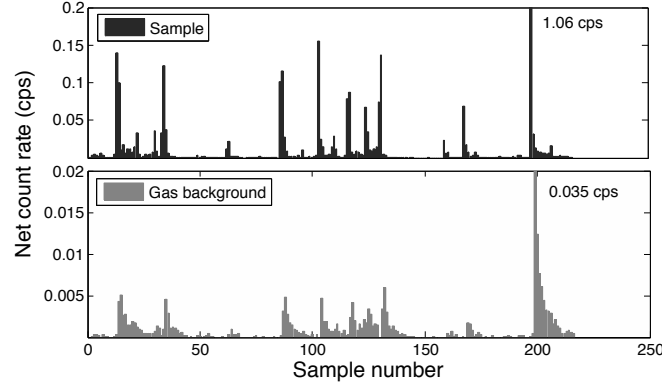
Figure 3.9: The memory effect illustrated through a series of sample (top), and gas background measurements (bottom). Note that the scales on the y-axes are different.

is above 0.035 cps has been used, in order to investigate how much of the sample activity is left in the cell in the subsequent gas background. The gas background measurements with residual activity from sample measurements further back in time are thus not included. The discrimination value was chosen by visually inspecting the data set shown in Figure 3.9.

The data has been fitted with a linear function, with a resulting slope of 0.032. A rough estimate of the memory effect, defined as fraction of the sample activity left in the cell in the following gas background measurement, is thus 3-4%.
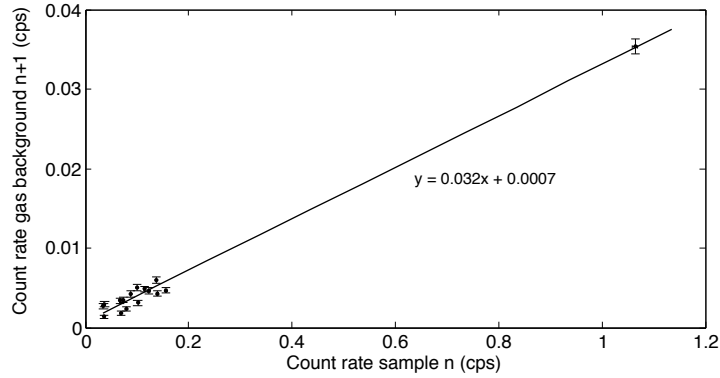
Figure 3.10: ^{133}Xe count rate in a series of gas background measurements, as a function of the count rate in the previous sample measurement.

As previously mentioned, the ultimate result of the memory effect is that it elevates the detection limit of the system, even if it is compensated for by subtraction of the gas background counts [3].

When it comes to the limits of detectability, there are two quantities that are of interest, the critical limit L_c, and the minimum detectable concentration, MDC.

The critical limit L_c is determined by the statistical fluctuations in the number of background counts in a given ROI. The net number of counts in an ROI is the total number of counts minus the background counts. If the net number of counts exceeds the L_c, it is assumed that some real activity is present in the sample [36, 31]. It is common to define L_c as the critical limit ensuring a false positive rate of no more than 5%, given by:

$$L_c = 2.33\sigma_{bg}, \tag{3.5}$$

where σ_{bg} is the standard deviation associated with the number of background counts.

The MDC is the real activity concentration needed to ensure a reasonably low false negative rate, given the critical limit L_c. Due to the statistical fluctuations always present in any counting system, the observed number of counts from a given source will vary around the true mean number of counts. The minimum value for the mean net number of counts c_{min}, that ensures a false negative rate of less than 5%, when L_c is defined according to Eq. 3.5, can be defined as [36]:

$$c_{min} = 4.65\sigma_{bg} + 2.71 \tag{3.6}$$

The MDC is calculated by substituting the net number of counts c in Eq 3.1 for c_{min}, and is thus given in mBq/m^3 [24].

A full derivation of Eq. 3.5 and 3.6 can be found in Refs. [31] and [36].

Figure 3.11 shows L_c of ^{133}Xe, as a function of the atmospheric ^{133}Xe concentration (C) in the previous sample measurement. Here the L_c is expressed as an atmospheric concentration, obtained by substituting c in Eq 3.1 for the L_c defined in Eq. 3.5. The data is taken from the same measurements as used in Figures 3.9 and 3.10.

In Figure 3.10 it was shown that in the case of only short term memory effect, the gas background depends linearly on the activity measured in the previous sample. If counting statistics is the only source of fluctuations in the background, σ_{bg} is given by the square root of the number of background counts. Since the background depends linearly on the sample activity concentration, it is reasonable to express L_c as a function of $\sqrt{C}$.

In Figure 3.11 the L_c data has been fitted with a first order polynomial, where $\sqrt{C}$ is the variable. The constant is included to account for the constant detector background not affected by C. Only the data where the activity concentration in the sample was above 2 mBq/m^3 was included in the fit, in order to remove data points where L_c is elevated due to long term memory effect from samples measured further back in time. These points are seen in the figure as high L_c values for very low concentrations. The discrimination limit was chosen through ocular inspection of the data set.

In the case of this SAUNA system located in Charlottesville, a typical sample contains a few mBq/m^3 of ^{133}Xe, which results in a critical limit between 0.1
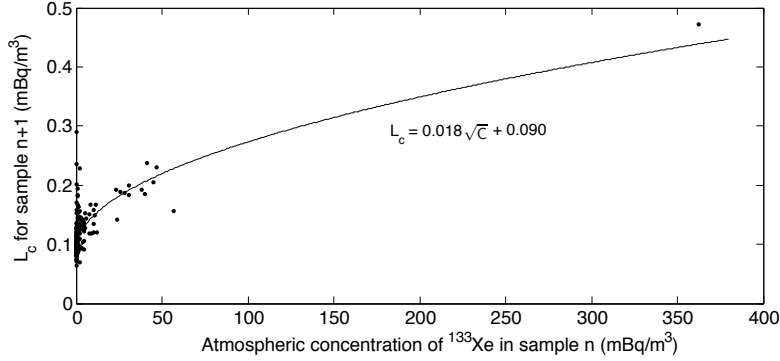
Figure 3.11: The critical limit for detection L_c as a function of the atmospheric activity concentration (C) of the previous sample. The line corresponds to a linear fit of L_c as a function of $\sqrt{C}$ for all samples with a concentration above 2 mBq/m³.

and 0.2 mBq/m³. As seen in Figure 3.11, a high sample activity of around 300 mBq/m³ increases this limit by almost a factor of 4.

The radioxenon detection systems used in the IMS are required to have an MDC of less or equal that 1 mBq/m³, for ^{133}Xe [34]. From Eqs. 3.5 and 3.6 it is seen that the MDC value is more than twice the value of L_c, and the high concentration in this data set thus results in an MDC very close to the required limit.

In order to assure a high reliability of the system it would thus be a great improvement if the memory effect could be removed. A lower detection limit would also result in lower uncertainties for the measured radioxenon concentrations, which could be important in order to identify the source of the radioactive gas, as described in Section 3.4.

In an ideal system with no memory effect, the gas background measurements would be obsolete. A memory effect reduction could thus allow for removal or reduction of the gas background measurements, leading to longer sample measurement times.

An additional motivation for memory effect reduction are the systems currently under development for use in On Site Inspections. Such systems are based on subsoil sampling close to a suspected nuclear explosion site. The amounts of radioactive xenon would thus be much higher than what is observed in the IMS systems, and the memory effect would therefor also be higher.

Finally, a system without memory effect would allow for recalibration or quality controls of the systems using radioactive gases. With the memory effect, such experiment would result in residual activity left in the detector for months.

There are various possible approaches for achieving a memory effect reduction. In Ref. [7] the plastic scintillator cell was exchanged for an inorganic cerium doped scintillator made of yttrium aluminum perovskite (YAP). This YAP cell presented a very small memory effect. However, with the detector geometry used, the X-rays at around 30 keV were absorbed in the YAP cell due

to its high effective atomic number. The X-rays could thus not be detected in the surrounding NaI(Tl) crystal, and a much thinner YAP cell would be needed for the technique to work.

Inorganic scintillating glass is another alternative material, but also this detector would need to be very thin in order to let the X-rays through.

Another possible solution is to saturate the plastic detector with stable xenon, so that there is no room for the radioactive atoms. This solution would however require incorporation of stable xenon exposure in the system processes in order to keep the cell saturated.

The approach that has been adopted in this work, is to coat the existing plastic scintillator cell with a material working as a gas diffusion barrier. An advantage with this solution is that it requires minimal changes of the existing system. The only thing that needs to be exchanged is the plastic scintillator cell. Provided that a barrier is achieved without impairing detector resolution and efficiency the analysis of the measurement data does no need to be altered either.

3.8   Surface coatings as diffusion barriers

The approach adopted in the work presented in this thesis is to coat the surfaces of the plastic scintillator exposed to the radioxenon sample with a material that is able to stop the xenon diffusion. This has previously been tested with pure metals that were deposited onto a plastic scintillator using electron beam lithography [7]. The problem with these coatings were that some of them easily flaked off, and that the light collection in the detector was impaired. For the work presented in this thesis the choice of coating materials was based on a number of desirable characteristics:

- The coating should be a good gas diffusion barrier.

- It should be transparent to the scintillator light, so that part of the signal is not lost in the coating. This requirement is fulfilled by materials having a band gap above 3.2 eV, which is the energy of 380 nm photons at the high energy end of the emission spectrum of BC-404 [37].

- The refractive index of the coating should be close to 1.58, which is the refractive index of BC-404, to minimize the risk of disturbing the light collection in the detector.

- The technique used to deposit the coating material should work at a relatively low temperature, since the softening point of the plastic scintillator material is as low as 70°C.

- The coating technique needs to be able to coat the inside of a cylinder with a uniform film. This requirement eliminates all coating techniques that requires line of sight.

Two transparent coatings were chosen for further investigation, Al_2O_3 deposited using Atomic Layer Deposition (ALD), and SiO_2 deposited with Plasma Enhanced Chemical Vapor Deposition. Both these coatings are used as gas diffusion barriers in a variety of applications. The materials have also previously

been deposited onto polymers in for example food packaging and organic light emitting devices [38, 39].

3.8.1 Atomic Layer Deposition

Atomic Layer Deposition (ALD) is a technique that is widely used to deposit thin films [40]. In this process the substrate to be coated is sequentially exposed to the reactant gases, which are called precursors.

The reactions between the surface of the substrate and the precursors are self-terminating, in the sense that only one atomic layer is deposited in each exposure, regardless of its duration (given that sufficient time is allowed for the surface to be covered with one layer). In Figure 3.12 the ALD process is illustrated in 4 steps.

Step 1: In the first step the substrate is exposed to the first precursor gas. The gas molecules reacts with the surface of the substrate an an atomic layer is formed.

Step 2: After the exposure of the first reactant the ALD reactor is flushed with an inert gas in order to remove excess precursor molecules, as well as by-products from the reaction. Since the substrate-precursor reaction is self-terminating, the substrate is left covered with one monolayer of molecules.

Step 3: The substrate is exposed to the second precursor gas which reacts with the surface.

Step 4: The excess precursor gas and reaction by-products are again removed from the ALD reactor. The result is a monolayer of the desired coating material.
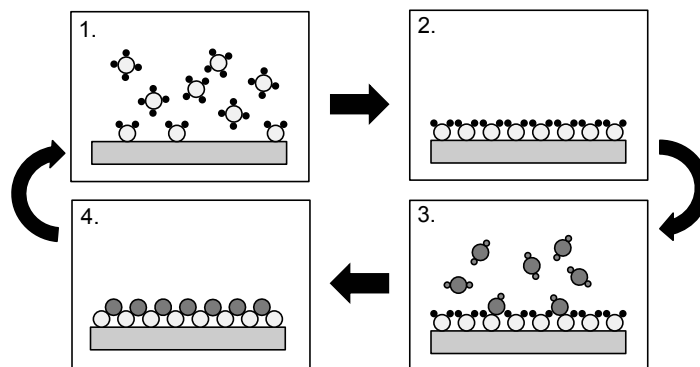
Figure 3.12: The ALD process.

This 4 step cycle is repeated until the desired film thickness is achieved, and the result is an amorphous film. The process is ideally linear with one monolayer of the film deposited in each cycle. Depending on the substrate this linearity is however often not achieved in the first cycles when the substrate material is still affecting the reaction.

One big advantage of the ALD process is that it is possible to coat very complex surfaces with a coherent film, and that very thin films can be achieved with high control over the coating thickness.

Depending on which type of film that is to be deposited, different precursor gases are used. In the case of the Al_2O_3 films made in this work the precursors are trimethylaluminum (TMA) and water.

One added advantage of the ALD technique for this particular application is that it has been proven to work at temperatures down to 33°C [41].

3.8.2 Plasma Enhanced Chemical Vapor Deposition

Plasma Enhanced Chemical Vapor Deposition (PECVD) is another widely used thin film deposition technique. In the PECVD process the substrate is exposed to a flow of mixed precursors in gas phase, and the reactivity of the gases is enhanced by the creation of a plasma [42]. PECVD can thus be performed at lower temperatures than conventional CVD where the reactivity is thermally increased. This is why PECVD is a better choice for applications where the substrate is sensitive to high temperatures.

One possible disadvantage of the PECVD technique is that it could be difficult for the plasma to reach into the plastic cylinder used in the SAUNA system, and cover it with a uniform film.

Further details about the PECVD process, and the equipment used to produce the coatings tested in this work, can be found in Ref. [43].

Chapter 4

Light transport properties of coated plastic scintillators

For the coating approach, described in Section 3.8, to be a viable solution to the memory effect problem, it is important that the resolution of the detector is not impaired by the coating. This is especially true since the two CE peaks at 129 and 199 keV from the decay of ^{131m}Xe and ^{133m}Xe needs to be sufficiently separated. There is a requirement of a resolution of the 129 keV CE peak below 40 keV for systems used in the IMS [34].

In this work, the resolution of the SAUNA beta detector is assumed to be dominated by photoelectron statistics, as well as variations in the detector response depending on the spatial location of the particle interaction. Both these factors are governed by the light collection in the detector, which can be studied independently of the rest of the detector setup, both through simulations and measurements.

Apart from the factors listed in Section 3.5.2, other possible contributors to the CE peak broadening in this particular system are:

- Mismatching between the two PM-tubes used to convert the light signal from the scintillator. Given equal quantum efficiencies of the two PM-tubes, and spatial symmetry in light collection efficiency, the gain of the two PM-tubes should ideally be the same [44].

- Self absorption in the xenon gas, due to interactions between the radiation to be detected and the xenon atoms. Normally the xenon sample in the cell is around 1.3 cm^3, of which the major part is stable xenon. The resolution of the 129 keV CE peak has been measured for such "normal" sample, containing a small amount of ^{131m}Xe, as well as a sample with no stable xenon, but the same radioactive content. The difference in the 129 keV CE resolution between the two measurements were only 1%.

In order to address this issue at an early stage in the project, as well as to find possible restrictions and recommendations for coating parameters, a study of the light collection was performed, by means of both simulations and

measurements. This study is described in Paper II and will also be summarized in the present chapter. At the end of the project, when a full detector had been coated, its resolutions was measured, and the results are presented in this chapter as well as in Paper III.

4.1 Simulations

4.1.1 Detect2000

Simulations were performed using the ray-tracing Monte Carlo code Detect2000 [45]. With this code it is possible to track individual photons as they travel through a user defined geometry. By defining the refractive indices and absorption lengths in all materials, as well as optical properties of all surfaces, light losses due to absorption or escape can be simulated. Photons are recorded as detected if they reach a surface defined as a photocathode. If the quantum efficiency of the photocathode is known it is then possible to determine the number of photoelectrons created for a given number of created scintillator photons.

The surface models used in the simulations were the POLISH and GROUND models that are implemented in Detect2000 [45]. When a photon encounters a surface it is first determined if it is to be reflected, or transmitted into the next medium. The probability for reflection is determined using Fresnel's formula:

$$R = \frac{1}{2}\left[\frac{sin^2(\theta_i - \theta_t)}{sin^2(\theta_i + \theta_t)} + \frac{tan^2(\theta_i - \theta_t)}{tan^2(\theta_i + \theta_t)}\right], \qquad (4.1)$$

where θ_i is the angle of incidence and θ_t is the transmission angle. The angles are defined with respect to the normal of a local micro-facet.

For the POLISH surface model this micro-facet is always parallel to the macro surface, and thus defines a totally smooth surface. The GROUND surface model represents a rough surface, and the normal of the micro-facet is sampled from a Lambertian distribution around the normal of the macro surface.

In both cases the complementary probability of transmission is given by $T = 1 - R$. The transmission angle is determined from Snell's law of refraction, and the photon can still be internally reflected if the angle of incidence is smaller than the critical angle for total internal reflection, defined in Eq. 3.4.

If the neighboring medium is vacuum, an external reflection coefficient can be defined, giving the probability that an escaped photon is reflected back into where it came from. The reflection angle is sampled from a Lambertian distribution, and the reflector is thus diffuse. This reflection coefficient can be used to simulate an external diffuse reflector, in this work the teflon tape that is wrapped around the detector.

4.1.2 Setup of simulations

The geometry of the plastic scintillator cell was implemented, with and without coating, as shown in Figure 4.1. Apart from the plastic scintillator material, optical pillows connecting the detector to the photocathodes of the PM-tubes were implemented, as well as an external diffuse reflector representing the teflon tape which is wrapped around a real detector. Photons were started from various
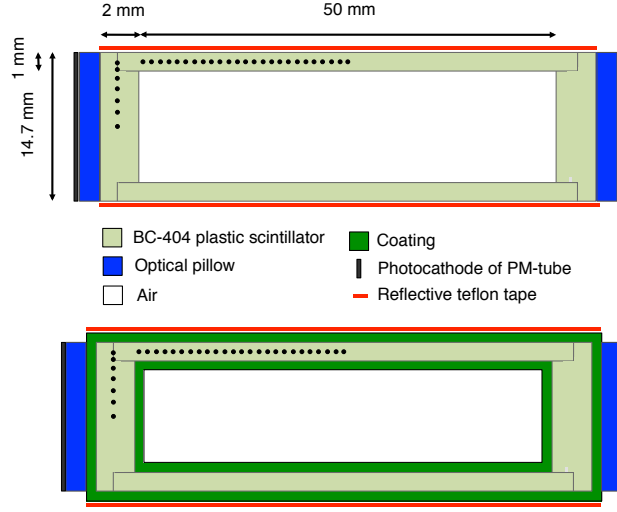
Figure 4.1: The implemented detector geometry without (top), and with (bottom) coating. The dots represents photon starting points.

positions in the geometry, so that the spatial dependence of the light collection efficiency could be evaluated. The starting points are shown in Figure 4.1.

Various simulations were performed, varying the thickness of the coating, its refractive index, and the quality of the surface of the plastic scintillator as well as the coating. Further details about the simulations can be found in Paper II.

4.1.3 Analysis and Results

Figure 4.2 shows the results from the simulations of an uncoated detector, with either a polished or a rough surface. The light collection efficiency ε was calculated as the fraction of all started photons reaching a PM-tube. It is seen that the surface quality of the plastic strongly affects the light collection, both when it comes to uniformity and the absolute value. Corresponding plots of the light collection efficiencies for coated detectors can be found in Paper II.

From the simulated light collection efficiencies, the resulting CE resolution at 129 keV was calculated for each simulated detector configuration, by using the expected light yield from such electrons and the quantum efficiency of the PM-tubes. The calculations only took into account the contributions from photoelectron statistics, and spatial variations in detector response. Other contributing factors are as previously mentioned, assumed to be minor compared to these.

In the calculations it was assumed that both contributions were gaussian, so that Eq. 3.3 and $FWHM = 2.35\sigma$ could be used.

For the contribution from photoelectron statistics this is a common assumption to do, since the number of created photoelectrons resulting from photons generated in a particular point in the detector, follows poisson statistics.

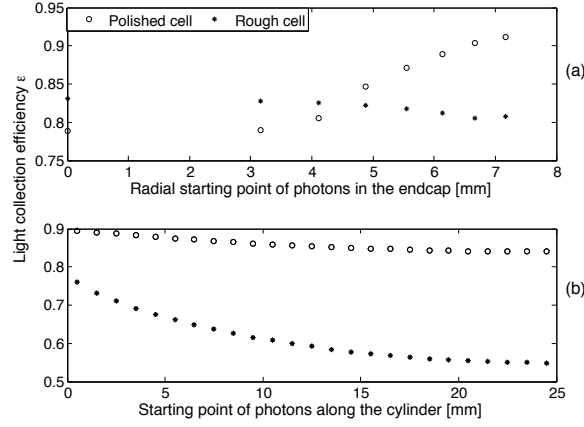For the contribution from spatial variations in the detector response, the

Figure 4.2: Light collection efficiencies as a function of photon starting point, in uncoated detectors with either polished of rough surfaces. (a) shows starting points in the endcap, and (b) starting points along the cylinder.

gaussian assumption is however a source of error, since the distributions are not gaussian. Figure 4.3 shows the distribution due to spatial variations, around the average light collection efficiency, for the two uncoated detectors.
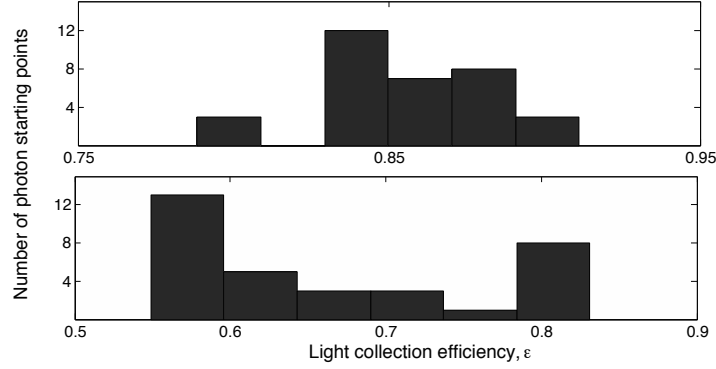

Figure 4.3: Distribution of the light collection efficiency depending on spatial variations in detector response. The top histogram is the distribution in a polished cell, and the bottom one the distribution in a rough cell.

A more detailed description of the calculations and the resulting resolutions for all simulated detector configurations, can be found in Paper II.

The main conclusions drawn from the simulations were:

- The light collection efficiency is highly dependent on the surface quality of both the plastic scintillator, and the coating. This is true both when it comes to the absolute efficiency, and the spatial variations.

36

- In the case of smooth surfaces the resolution is dominated by the photo-electron statistics, and when rough surfaces are involved spatial variations is the dominating contribution.

- A coating with a rough surface impairs the light collection, regardless of the quality of the plastic surface. However, if a smooth coating is achieved on a rough plastic surface, the light collection can be improved by the coating.

- A good optical match between the refractive indices of the plastic scintillator and the coating is important. Furthermore, it is preferable that the refractive index of the coating is higher than the one of the plastic, rather than lower.

- For the coating thicknesses below 1 μm simulated here, the light collection efficiency is not significantly dependent on the coating thickness.

To summarize, it was found that if a smooth coating with a refractive index close to the one of the plastic is achieved, the light collection efficiency is not expected to be significantly impaired.

The roughness of a flat scintillator sample was later studied using Atomic Force Microscopy (AFM), both before and after it was coated with 210 nm Al_2O_3. Figure 4.4 shows the results from these measurements, and it is clearly visible that the coating has a smoothening effect on the scintillator surface. This is very promising from a light collection point of view.
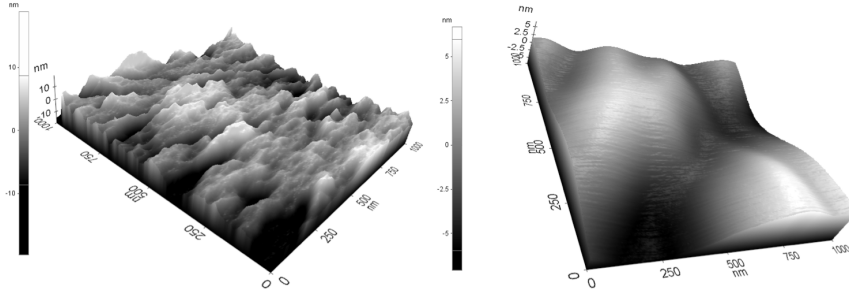
Figure 4.4: AFM pictures of a BC-404 sample before (left) and after (right) coating with 210 nm Al_2O_3.

Another observation from the simulations were that for the polished cell, the light collection efficiency was lower in the endcaps than in the cylinder (see Figure 4.2), even though the endcaps are closer to the PM-tubes. The loss of light was found to occur in the optical pillows, which are not wrapped in teflon tape. If the reflective tape was extended to cover also the optical pillows in the simulations, the light collection efficiency from starting points in the endcaps were found to be higher, and also more uniform.

It should be noted that the surface properties used in the simulations are two extremes. It is not likely that a real detector is well described by either of these. This was also confirmed by comparing the calculated resolutions for uncoated detectors with real measurements. Normal CE resolutions of SAUNA

systems in operation lie between the two simulated extremes, indicating that a real cell might be better described by something in between the POLISH and GROUND surface models used here. However, the purpose of the simulations was not to exactly reproduce the performance of a real detector, but rather to investigate if the light collection efficiency would be impaired by a coating. It is believed that this was captured despite the simplified surface models.

An additional shortcoming of the simulation code is that it does not account for thin film interference, which could be an issue since the proposed coating thicknesses are of the same order of magnitude as the wavelength of the scintillator light.

4.2   Measurements on a simplified geometry

In addition to the simulations, measurements were conducted in order to evaluate how the interactions between the scintillating photons and the scintillator surface would be affected by a coating. This was done by using a simplified geometry of flat plastic scintillator samples with the dimensions $30\times20\times100$ mm. The idea was to se if the amount of internally reflected light would change if a sample was coated. For the measurement, some samples were coated with 20 or 70 nm of Al_2O_3 using ALD at 45 or 65°C. Some samples were only heated to these temperatures without being coated, in order to see if the heating itself was responsible for any damage. Finally, some samples were left uncoated. All samples were measured both before, and after the coating/heating procedure.

4.2.1   Measurement setup

The measurements consisted in sending light into one end of the sample and then measure what came out at the other end. Light of specific wavelengths was created by passing white light through a diffraction grating. A schematic picture of the measurement setups is shown in Figure 4.5. Two different setups were used, chosen to assure that at least part of the light would undergo some surface interactions.

The first approach was to use light of a wavelength within the absorption spectrum of the scintillator, and in that way create scintillating light emitted in all directions, assuring that part of it would interact with a surface.

The other approach was to use visible light but, letting it hit the sample at a certain angle, and in that way increase the probability of surface interactions.
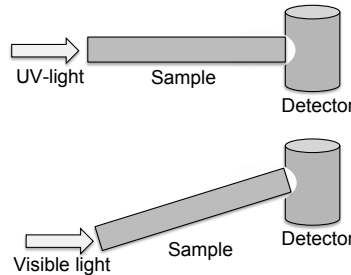

Figure 4.5: Schematic view of the experimental setup used in the measurements.

4.2.2 Results

The qualitative conclusions that could be drawn from the measurements were that no drastic optical degradation of the plastic scintillator samples occurred by coating them, and that the null hypothesis of no degradation at all can not be ruled out, which are both results in favor of the coating approach.
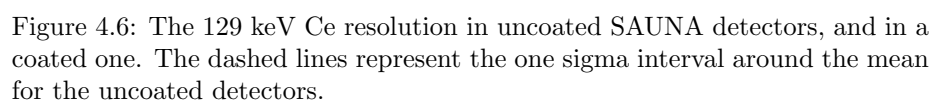
It was unfortunately not possible to draw any quantitative conclusions. The measurements were performed various times, and it was difficult to reproduce the results. An explanation for this could be that the systematical errors were larger than the statistical ones, as well as the differences in performance between the different samples. Possible systematical errors included difficulties in positioning the sample at the exact same position relative to the light source and the detector, as well as possible damage to the samples while handling them during and between the measurements.

4.3 Measurements with a complete detector

At the end of this project one complete detector was coated with 425 nm Al_2O_3. In Chapter 5 measurements of the memory effect in this detector are described. In this section measurements of the resolution of this coated detector are described. Further details about the measurement can be found in Paper III.

The coated detector was mounted in a SAUNA NaI(Tl) crystal and coupled to PM-tubes and the setup was operated in beta gamma coincidence mode. Further details about the setup can be found in Paper III, and Chapter 5.

The resolution of the detector was measured by introducing ^{131m}Xe into the detector, and subsequent analysis of the measured 129 keV CE peak. The measurement was done twice, with 2.5 months separation. In Figure 4.6 the resulting resolutions are shown, together with the 129 keV CE resolutions in operational SAUNA systems. The IMS systems are required to have a resolution no larger than 40 keV at this energy [34]. The CE resolution at 129 keV of the full coated detector was around 33 keV in both measurements. This value is below the mean resolution of uncoated detectors, and within the resolution interval presented by these.

Figure 4.6: The 129 keV Ce resolution in uncoated SAUNA detectors, and in a coated one. The dashed lines represent the one sigma interval around the mean for the uncoated detectors.

Chapter 5

Memory effect in coated plastic scintillators

This chapter presents measurements performed to evaluate the ability of Al_2O_3, and SiO_2 coatings to reduce xenon diffusion, and hence the memory effect. Further details on the performed experiments and results can be found in Paper I and Paper III. Paper I describes measurements performed on flat plastic scintillator samples, and Paper III describes similar measurements conducted using a complete detector coated with the most promising coating identified in Paper I.

5.1 Coatings

Several flat plastic scintillator samples, with the same geometry as the endcaps in the complete detector (see Figure 5.1) were coated with Al_2O_3, or SiO_2. The samples were either of the material BC-444, or BC-404.

The BC-444 samples were milled from a cast scintillator sheet to the desired geometry, and the BC-404 samples were ordered from the normal manufacturer of the detectors used in the SAUNA systems. The thicknesses of the coatings varied between approximately 20 and 400 nm. Further details on the different samples can be found in Paper I.

All parts of one complete detector, as shown in Figure 5.1 were coated with 425 nm Al_2O_3, since this was found to be the most promising coating.

The Al_2O_3 coatings were made with ALD at the Department of Materials Chemistry, Uppsala University, and later by the private company Nanexa AB. The SiO_2 coatings were made using PECVD, at the Microelectronics Research Center, University of Texas at Austin, USA.

5.2 Experimental: flat endcap samples

The measurements of the memory effect in flat samples were conducted independently at FOI in Sweden, and at the University of Texas at Austin in USA. In this chapter only the measurements performed at FOI will be described, and a detailed description of the measurements conducted in Texas can be found in Ref. [43]. Further details abut all measurements can be found in Paper I.
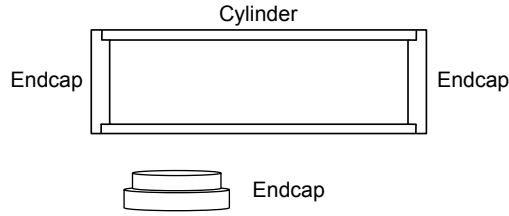
Figure 5.1: Schematic picture of the parts of the plastic scintillator cell, which consists of a hollow cylinder and two endcaps.
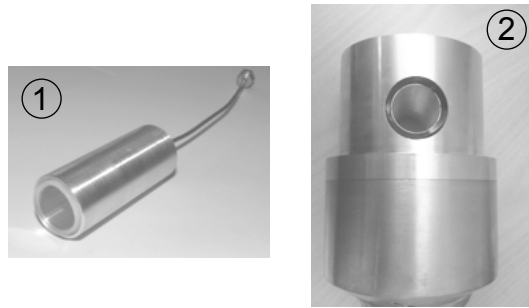

Figure 5.2: The aluminum cell with a plastic endcap attached to its open end (1). The cell was introduced into the drilled hole in the NaI(Tl) crystal (2).

The approach adopted for the experiments performed at FOI was to expose both coated and uncoated plastic samples to radioactive xenon, and then measure the residual activity in the plastic after the exposure. The memory effect could then be calculated as the fraction of the exposure activity that was left in the cell as residual activity.

The plastic samples were glued onto open-ended aluminum cylinders, in order to create a gas tight cell.

The cell was connected to a gas transfer system built for the purpose of the experiment, through which gases could be transferred into the cell. The system also incorporated a micro pump which was used to evacuate the cell. The pressure inside the cell was monitored by a pressure sensor.

The cell was placed inside the well of a SAUNA NaI(Tl) detector which was used for activity measurements. Pictures of the aluminum cell and the NaI(Tl) detector are shown in Figure 5.2.

The measurement of the memory effect in each sample was carried out by introducing around 7 kBq of ^{133}Xe into the cell, along with helium to a pressure of around 0.9 bar. The gas was then left in the cell for a 7 hour exposure. During this time the activity of the injected gas was measured. After the exposure the gas was evacuated through repeated pumping and flushing with helium. After the sample evacuation the residual activity in the cell was measured during at least 15 hours. The activity measurements were done using the NaI(Tl) detector,

measuring gamma radiation from the decay of ^{133}Xe.

Two samples with each coating material and thickness were measured, as well as three uncoated samples. In addition, an Al sample was measured in the same way, and was used to estimate the lower limit of the memory effect that could be measured using this technique.

5.3 Experimental: complete detector

The coated parts of the full detector were assembled using optical cement, wrapped in reflective teflon tape and placed in a light tight housing.

The memory effect in the full detector was measured in three slightly different ways, all based on the exposure to ^{133}Xe.

The first measurement was the same as the one described in the previous section, with the aluminum cell exchanged for the full detector and its housing. This measurement was done so that the results from flat samples and a full cell could be compared without having to consider possible systematical errors.

In the following measurements the cell was coupled to PM-tubes and the measurements were done in beta-gamma coincidence mode, using both the NaI(Tl) and the plastic scintillator itself. This setup allowed both to measure the memory effect, and the resolution of the detector. The coincidence measurements were performed twice, with different pump-and-flush cycles.

The procedure of the measurements was the same as described in Section 5.2, with the exception that a much lower activity was introduced into the cell in the beta-gamma measurements, since the detector background is drastically reduced with this technique.

Figure 5.3 shows the different parts used in the mounting of the detector.
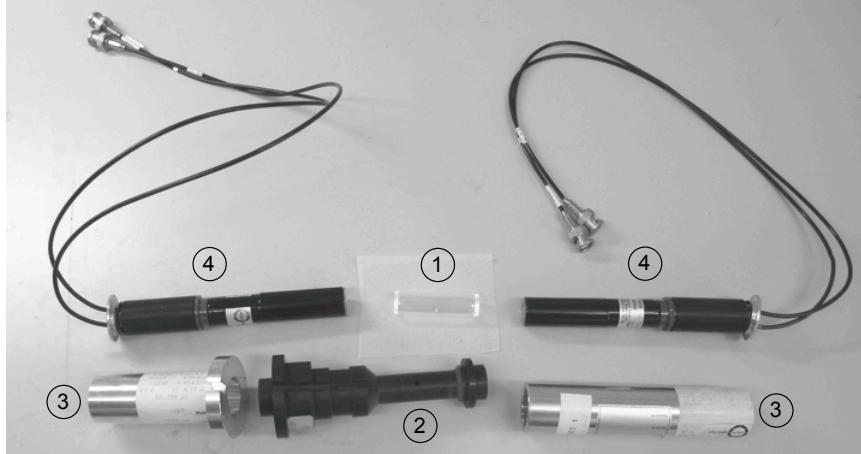

Figure 5.3: The different parts of the mounted detector. ① is the cell, before being wrapped in teflon tape. The cell is inserted in a light tight housing, ②. Two supports ③ are used to keep the PM-tubes ④ in place.

5.4 Analysis

In all measurements, the decay branch of ^{133}Xe characterized by a beta endpoint energy of 346 keV together with an 81 keV gamma ray, was used in the analysis (see Section 3.2). The analysis procedure and calculation of the memory effect was slightly different if only a gamma spectrum was recorded, or if the detector was operated in beta-gamma coincidence mode. In either case the final memory effect was calculated as the ratio between the exposure activity, A_{expo} and the residual activity A_{resid} according to:

$$ME = \frac{A_{resid}e^{\lambda t_d}}{A_{expo}},$$ (5.1)

where the factor $e^{\lambda t_d}$ is decay correcting the residual activity for the time, t_d, between the start of the two measurements, and λ is the decay constant of ^{133}Xe.

The activities at the start of each measurement were calculated according to:

$$A = \frac{\lambda N}{\varepsilon\gamma(1 - e^{-\lambda t_{real}})}$$ (5.2)

where γ is the branching ratio of the decay, t_{real} is the real data acquisition time, ε is the absolute detection efficiency, and N is the dead time corrected detected number of counts corresponding to the decay in question.

The absolute detection efficiency was different in the exposure measurement and in the residual activity measurement. During the exposure the activity was distributed in the gas contained in the cell, but the residual activity was located only in the walls of the cell. The absolute detection efficiency in each case was calculated using MCNP5 [46].

5.4.1 Gamma spectra

For the gamma spectra the number of counts, N, were determined from the area of the 81 keV gamma peak. The exposure and residual activity spectra from each measurement were very different in terms of the sample activity, and were therefore treated differently in the analysis.

The spectra recorded during the exposure measurement contained very large peaks which were easily distinguished from the detector background. The peaks were fitted with a peak shape $P(x)$ composed of a gaussian $G(x)$, and a tail function $T(x)$ defined as:

$$P(x) = G(x) + T(x) =$$
$$= \frac{A}{\sqrt{2\pi}\sigma}exp\left(-\frac{(x - x_0)^2}{2\sigma^2}\right) +$$
$$+ AH_texp\left(\frac{x - x_0}{T_s\sigma}\right)erfc\left(\frac{x - x_0}{\sqrt{2}\sigma} + \frac{1}{\sqrt{2}T_s}\right),$$ (5.3)

where $erfc$ is the complementary error function defined by:

$$erfc(x) = \frac{2}{\sqrt{\pi}} \int_x^{\infty} e^{-t^2} dt \qquad (5.4)$$

The tail function $T(x)$ represents events with incomplete charge collection. The fit parameters where the area of the gaussian peak A, its standard deviation σ, and the centroid x_0. H_t is related to the height of the tail function, and T_s its slope [47]. Both H_t and T_s were set to fixed values common for all measurements.

Together with the peak shape function, a second order polynomial background was included in the fit.

The analysis of the residual activity measurements was further complicated by the sometimes very low activities, in combination with a background peak at approximately the same position as the ^{133}Xe 81 keV gamma peak.

To obtain a peak area related to the decay under study despite these difficulties, a detector background histogram was included in the fit. The background used was measured for a period of 14 days, and thus had good statistics.

Apart from the fit parameters in the peak shape $P(x)$, a scaling factor and a shift factor for the background histogram were fitted. The shift parameter was used since the measurements were conducted over the course of several months, and small drifts in the energy scale were observed during this time.

The analysis described in this section was used to analyze all the measurements of endcaps, and the first measurement of the memory effect in the full detector.

5.4.2 Beta-gamma coincidence spectra

The beta-gamma spectra measured using the full coated detector were analyzed in a different way. Instead of fitting a function to a peak, the number of counts in a region of interest (ROI) covering the decay of interest, were used. The analysis is based on the Net Count Calculation method which is used to analyze SAUNA IMS data [24, 25].

The ROI included the 81 keV gamma peak in coincidence with the beta distribution with endpoint energy of 346 keV (corresponding to ROI3 in Figure 3.4).

The ROI also contains background counts which needs to be subtracted before calculating the activity according to Eq. 5.2. The background contains two components. The first is a constant background that is determined by the ambient background radiation at the location of the system, referred to as the detector background. The second component is a gas background which contains ^{133}Xe memory effect from previous measurements. The latter component is not constant in time, but will decrease due to decay. Figure 5.4 shows the components present in each measurement. The area under the activity graphs correspond to the number of counts from each contribution in each measurement.

To calculate the memory effect, 4 measurements were used in the analysis:

Detector background: A background measured during 8 days before the detector had been exposed to any activity. The same detector background was used in the analysis of all measurements.
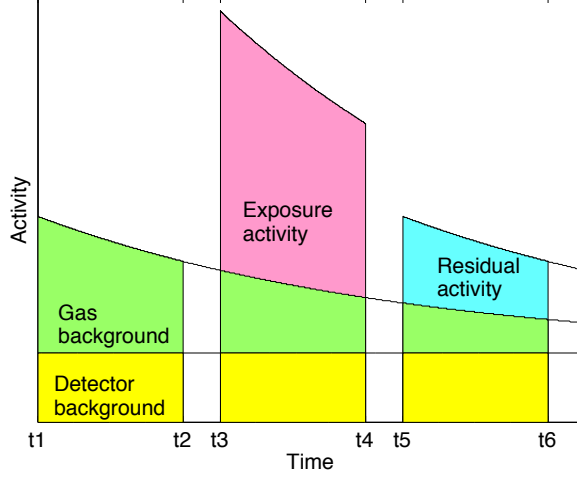
Figure 5.4: Schematic view of the different activity components in each measurement. The residual activity measurement will be the gas background for the subsequent measurement.

Gas background: A measurement of an empty cell, containing residual activity from previous measurements, in addition to the detector background. The activity in this measurement that exceeds the constant detector background decreases in time according to the decay constant of ^{133}Xe.

Exposure measurement: Measurement of the exposure activity, together with the detector background and residual activity from previous measurements.

Residual activity measurement: Measurement of the residual activity left in the cell after the exposure, together with the detector background, and a contribution from the memory effect already present in the cell before the exposure measurement.

The activity values that were used in Eq. 5.1 were the exposure activity, A_{expo}, at the start of the exposure measurement, and the residual activity, A_{resid}, at the start of the residual activity measurement. The respective start times are indicated by t3 and t5 in Figure 5.4.

The net number of counts, N_{expo} and N_{resid}, were calculated from the measured number of counts, S_{expo} and S_{resid}, by subtraction of both detector background and gas background counts.

The background subtraction was performed according to:

$$N = S - \frac{t_{real}^S}{t_{real}^D} D - e^{-\lambda\tau} \frac{(1 - e^{-\lambda t_{real}^M})}{(1 - e^{-\lambda t_{real}^M})} \left(M - \frac{t_{real}^M}{t_{real}^D} D \right), \qquad (5.5)$$

where D and M are the number of counts in the detector background, and gas background measurements, respectively. t_{real} are the real data acquisition

46

times in each measurement. The factor $e^{-\lambda\tau}$ is used to correct for decay of the gas background activity from the start of the gas background measurement to the start of the sample measurement. τ is thus either the time interval between t1 and t3, or the time between t1 and t5, for the exposure and residual activity, respectively.

5.5 Results and discussion

5.5.1 Endcaps

In Figure 5.5 the results from the memory effect measurements of endcaps are shown. The uncertainties in the memory effect values were calculated by propagating the uncertainties in the peak areas, as well as in the dead time correction factor, into the final result.
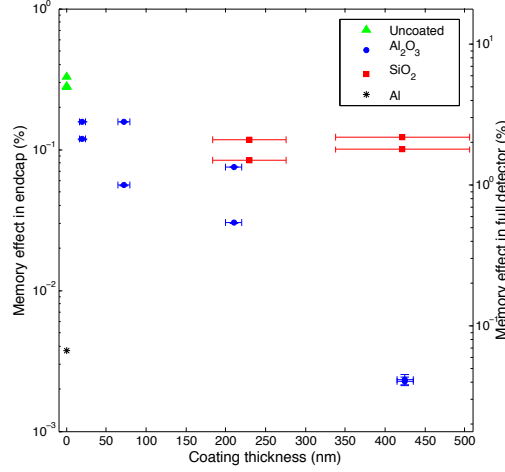
Figure 5.5: Results from the memory effect measurements of flat plastic scintillator samples. The values are given as the percentage of exposure activity left in the cell after sample evacuation. The left y-axis shows the measured memory effect, and the right y-axis shows the expected memory effect in a complete detector, taking into account the different surface areas of the two cases. The error bars in the y-direction includes statistical errors only, and are included for all data points but not visible for all. The error bars in the x-direction corresponds to the uncertainties in the determination of the coating thicknesses. Note that the scale on the y-axes is logarithmic.

Measurements were conducted on both coated and uncoated samples, as well as a plain Al sample used to estimate the smallest plastic related memory effect that could be measured using this method. All the measurements shown in the figure correspond to individual samples, and each sample was only measured once.
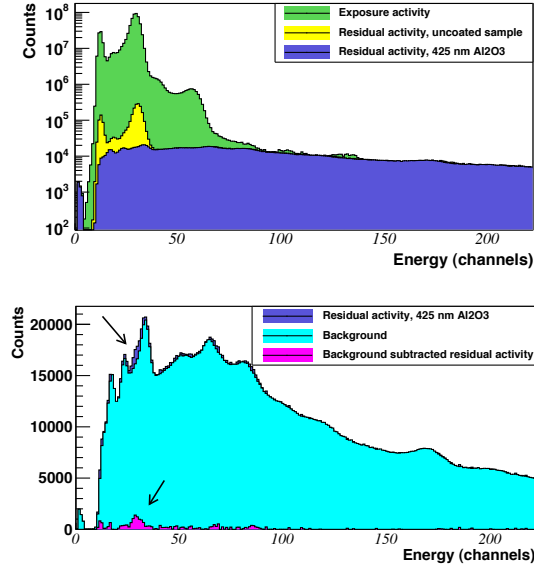
Figure 5.6: Examples of the measured gamma spectra. In each panel all spectra are scaled to the same live time.
Top: Exposure spectrum (green), residual activity in an uncoated sample (yellow), and the residual activity in a sample coated with 425 nm Al_2O_3 (blue).
Bottom: The same residual activity in a coated sample as in the top panel (blue) but on a linear scale, together with a background spectrum (cyan). Shown is also the residual activity when the background has been subtracted from the blue spectrum (magenta). The arrows indicate the residual activity corresponding to the memory effect in a sample coated with 425 nm Al_2O_3.

It is seen that all coated samples have a lower memory effect than the uncoated ones. For the Al_2O_3 samples, a decreased memory effect with increasing coating thickness can be observed. The thickest Al_2O_3 coatings of 425 nm show a memory effect lower than what is seen in a plain Al sample, indicating that almost no Xe has diffused into the plastic scintillator material. The memory effect using this thickness is a factor of 100 lower than what was observed in the uncoated samples. The SiO_2 coatings did not show as good diffusion barrier properties as the Al_2O_3 coatings.

Shown are also the expected memory effect in a complete detector, which has been estimated by scaling the measured memory effect with the difference in surface area between the two cases. The memory effect in an uncoated complete detector is from these measurements expected to lie around 5%, which is in quite good agreement with what is usually observed in the operational SAUNA systems.

It should be noted that for some coating thicknesses the results differ quite a lot between the two measured samples of the same type. One reason for this could be cracks or other imperfections of the samples affecting the results.

In Figure 5.6 some example spectra are shown. It is from this picture clearly visible how extremely low the memory effect in the sample coated with 425 nm

Al$_2$O$_3$ is. It is almost not possible to distinguish the excess activity from the detector background. In the exposure spectrum sown in the figure, a chance coincidence peak can be observed. The counts in this peak are not accounted for in the analysis, and thus adds a systematical error to the results.

5.5.2 Complete detector, and a comparison between all measurements

Figure 5.7 shows the exposure and residual activity measured in the full coated detector. Also from this picture it is clear that the memory effect in the coated detector is very small.
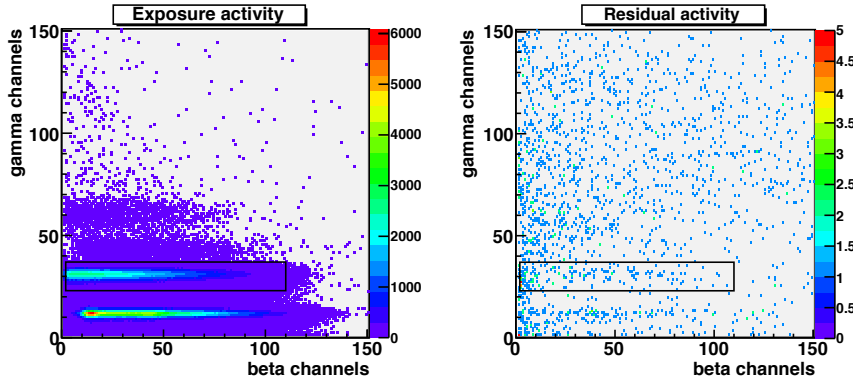
Figure 5.7: Beta-gamma coincidence spectra measured using the full coated detector. Left: 7 hour measurements of the exposure activity. Right: 44 hour measurement of the residual activity. The black rectangles correspond to the ROIs used in the analysis. Note that the scales are different in the two plots.

In Table 5.1 the memory effects from the three measurements of the full coated detector, are compared to the measurements of the endcaps. It is seen that the memory effect in a full detector estimated from measurements of coated endcaps, is a factor of 10 higher than what was measured in the complete coated detector.

The memory effect measured in the full coated detector is a factor of 1000 lower than what is usually seen in operational systems. One explanation for this discrepancy between measured and estimated values, could be that the very small memory effect in these measurements is related to something other than the actual plastic. The measurement of the Al endcap support this reasoning, since the memory effect in this sample is of the same order of magnitude as in the 425 nm Al$_2$O$_3$ coated plastic sample. This indicates that the low measured residual activity in all these cases are radioxenon left in other parts of the experimental setup, for example the glue used to assemble the cell.

The two beta-gamma coincidence measurements of the memory effect in the full detector are consistent, with overlapping errors, indicating that the different pump-and-flush cycles used does not affect the memory effect much. However, the memory effect in the full detector measured in gamma mode was a factor

Table 5.1: Memory effects in endcaps and full detector. All coatings are 425 nm Al_2O_3. The estimated memory effects in a full detector are calculated from the measurements of endcaps by scaling with the difference in plastic surface area exposed to radioxenon. It should be noted that the three measurements on a full detector were done on one singe detector, while the measurements of the endcaps are all individual samples.

Sample	Measurement technique	Measured memory effect in sample (%)	Estimated memory effect in full detector (%)
Full coated detector	γ	0.0048 ± 0.00016	0.0048 ± 0.00016
	$\beta - \gamma$	0.0019 ± 0.00041	0.0019 ± 0.00041
	$\beta - \gamma$	0.0025 ± 0.00042	0.0025 ± 0.00042
Uncoated endcap	γ	0.28 ± 0.0014	5.0 ± 0.024
	γ	0.33 ± 0.0015	5.9 ± 0.026
	γ	0.28 ± 0.0012	5.0 ± 0.021
Coated endcap	γ	0.0023 ± 0.00014	0.041 ± 0.0025
	γ	0.0023 ± 0.00022	0.041 ± 0.0038
Al endcap	γ	0.0037 ± 0.00013	n.a.

of two higher than the beta-gamma coincidence measurements. The reason for this difference is not known.

It should be noted that all memory effects measured in this work are slight underestimations of the memory effect expected in a real system. The reason is that during the experiments the exposure time was only 7 hours, but in a real system the samples are measured for 11 hours.

5.5.3   Degradation in time

For the coatings to be a viable solution to the memory effect, it is important that they maintain their quality for a longer period of time. Measurements of both the resolution and the memory effect of the full coated detector were performed with 2.5 months separation, and during this time no degradation of either of the qualities were observed.

However, for the coated endcaps, the coatings on some samples started to crack after some time, and re-measurement of these samples also showed an elevated memory effect. As mentioned in Section 5.1, the measured endcaps were both BC-404 endcaps identical to the ones used in the SAUNA system, and BC-444 endcaps fabricated in a workshop from a cast sheet of scintillator material. It was the BC-444 endcaps that presented the degradation. One explanation could be that there is some residual stress from the milling of these samples, causing the coatings to crack. Further investigations are however needed in order to find out the reason for the degradation, and to evaluate if it might be a problem also for the BC-404 endcaps and the cylinder.

Chapter 6

Conclusions and outlook

In this work we have proposed and demonstrated a solution to the memory effect problem in the radioxenon detection systems used within the verification regime of the CTBT. The proposed solution consist in coating the plastic scintillator detector in a transparent coating. In this work Al_2O_3 has been proven to be a good coating material for this application.

Measurements of the memory effect in a detector coated with 425 nm Al_2O_3, showed a memory effect reduction of a factor of 1000 compared to what has previously been observed in uncoated detectors. It was also shown that the resolution of this detector was comparable to uncoated detectors.

If these qualities can be maintained for a longer period of time, and be reproduced, it is believed that this approach would be a viable solution to the memory effect problem in the SAUNA system.

Further steps that need to be taken before using coated detectors in the field, is to evaluate the long term performance of the detector as well as to investigate the reproducibility of the method. The measurements conducted in this work are based on one single full coated detector.

The light collection simulations showed that if a smooth coating is achieved, with a refractive index close to the one of the plastic, the detector resolution is not expected to be significantly degraded by the coating. It was seen from AFM pictures, that the coating does have a smoothening effect on the plastic surface, which is a promising result. Measurements of the full detector also showed a good detector resolution. However, since the resolution measurement was only performed on one single detector, it is difficult to draw any conclusions on the effect of the coating on the resolution. The resolution has been shown to vary between individual detectors, depending on the quality of the plastic scintillator, and it is not clear how this particular one would have performed without the coating.

In order to investigate this further it would be needed to measure the resolution with another technique, that does not require the detector to be assembled to a gas tight cell. A radioactive point source could be used outside the detector, which in that case would not have to be glued together. This approach would allow to measure the same detector both before and after coating deposition. One could also measure the resolution as a function of position of the source and in that way evaluate the dependence on spatial variations in detector response. Such measurements could also be used as input to simulations, in order to find

more realistic surface settings.

The coating thickness of 425 nm is larger than what is used for gas diffusion reduction in other applications. In order to investigate the reason for this it is planned to perform molecular dynamics simulations on Al_2O_3 exposed to xenon, as well as the plastic/Al_2O_3 system exposed to xenon. Such calculations could help in further optimization of the method.

Acknowledgements

Bibliography

[1] www.ctbto.org/.

[2] Marc Bean, Nadereh St-Amant, and R. Kurt Ungar. Understanding the memory effect in SAUNA's plastic scintillator and its impact on the measurement, poster presented at noble gas workshop in nevada, USA, Nov 2007.

[3] Brian D. Milbrath, Matthew W. Cooper, Lance S. Lidey, Theodore W. Bowyer, James C. Hayes, Justin I. McIntyre, Lynn Karr, David Shafer, and Jeff Tappen. Radioxenon atmospheric measurements in north Las Vegas, NV. In *29th Monitoring Research Review: Ground-Based Nuclear Explosion Monitoring Technologies*, 2007.

[4] Paul R. J. Saey, Theodore W. Bowyer, and Anders Ringbom. Isotopic noble gas signatures released from medical isotope production facilities - simulations and measurements. *Applied Radiation and Isotopes*, 68:1846–1854, 2010.

[5] Martin B. Kalinowski and Christoph Pistner. Isotopic signature of atmospheric xenon released from light water reactors. *Journal of Environmental Radioactivity*, 88:215–235, 2006.

[6] A. Ringbom, T. Larsson, A. Axelsson, K. Elmgren, and C. Johansson. SAUNA - a system for automatic sampling, processing, and analysis of radioactive xenon. *Nuclear Instruments and Methods in Physics Research A*, 508(3):542–553, 2003.

[7] Carolyn E. Seifert, Justin I. McIntyre, Kathryn C. Antolick, April J. Carman, M. W. Cooper, James C. Hayes, Tom R. Heimbigner, Charles W. Hubbard, Kevin E. Litke, Mike D. Ripplinger, and Reynold Suarez. Mitigation of memory effects in beta scintillation cells for radioactive gas detection. In *27th Seismic Research Review: Ground-Based Nuclear Explosion Monitoring Technologies*, 2005.

[8] L. Bläckberg, A. Ringbom, H. Sjöstrand, and M. Klintenberg. Assisted self-healing in ripped graphene. *Physical Review B*, 82(19):195434, Nov 2010.

[9] Thomas Jonter. Nuclear non-proliferation - a brief historical background. In G. Janssens-Maenhout, editor, *Nuclear Safeguards and Non-Proliferation*. 2008.

[10] http://www.iaea.org/about/history.html.

[11] http://www.iaea.org/newscenter/focus/npt/index.shtml.

[12] www.un.org/disarmament/WMD/nuclear/npt.shtml.

[13] http://www.un.org/disarmament/WMD/nuclear/npttext.shtml.

[14] Anders Ringbom. Nuclear treaty verification at foi, annual report 2008. Technical Report FOI-R-2790–SE, Swedish Defence Research Agency, FOI, 2009.

[15] M. Auer, A. Axelsson, X. Blanchard, T. W. Bowyer, G. Brachet, I. Bulowski, Y. Dubasov, K. Elmgren, J. P. Fontaine, W. Harms, J. C. Hayes, T. R. Heimbigner, J. I. McIntyre, M. E. Panisko, Y. Popov, A. Ringbom, H. Sartorius, S. Schmid, J. Schulze, C. Schlosser, T. Taffary, W. Weiss, and B. Wernsperger. Intercomparison experiments of systems for the measurement of xenon radionuclides in the atmosphere. *Applied Radiation and Isotopes*, 60:863–877, 2004.

[16] Yu. V. Dubasov, Yu. S. Popov, V. V. Prelovskii, A. Yu. Donets, N. M. Kazarinov, V. V. Mishurinskii, V. Yu. Popov, Yu. M. Rykov, and N. V. Skirda. The APIKC-01 automatic facility for measuring concentrations of radioactive xenon isotopes in the atmosphere. *Instruments and Experimental Techniques*, 48(3):108–114, 2005.

[17] P. L. Reeder, T. W. Bowyer, and R. W. Perkins. Beta-gamma counting system for Xe fission products. *Journal of Radioanalytical and Nuclear Chemistry*, 235(1–2):89–94, 1998.

[18] J.-P. Fontaine, F. Pointurier, X. Blanchard, and T. Taffary. Atmospheric xenon radioactive isotope monitoring. *Journal of Environmental Radioactivity*, 72:129–135, 2004.

[19] C. R. Carrigan, R. A. Heinle, G. B. Hudson, J. J. Nitao, and J. J. Zucca. Trace gas emissions on geological faults as indicators for underground nuclear testing. *Nature*, 382:528–531, Aug 1996.

[20] Kenneth S. Krane. *Introductory nuclear physics*. John Wiley & Sons, 1988.

[21] T. W. Bowyer, C. Schlosser, K. H. Abel, M. Auer, J. C. Hayes, T. R. Heimbigner, J. I. McIntyre, M. E. Panisko, P. L. Reeder, H. Satorius, J. Schulze, and W. Weiss. Detection and analysis of xenon isotopes for the comprehensive nuclear-test-ban treaty international monitoring system. *Journal of Environmental Radioactivity*, 59:139–151, 2002.

[22] www.nucleide.org.

[23] P. L. reeder, T. W. Bowyer, J. I. McIntyre, W. K. Pitts, A. Ringbom, and C. Johansson. Gain calibration of a β/γ coincidence spectrometer for automated radioxenon analysis. *Nuclear Instruments and Methods in Physics Research A*, 521:586–599, 2004.

[24] Anders Axelsson and Anders Ringbom. Xenon air activity concentration analysis from coincidence data. Technical Report FOI-R–0913–SE, Swedish Defence Research Agency, FOI, 2003.

[25] Lars-Erik De Geer. The xenon NCC method revisited. Technical Report FOI-R–2350-SE, Swedish Defence Research Agency, FOI, 2007.

[26] Richard W. Perkins and Leslie A. Casey. Radioxenons: their role in monitoring a comprehensive test ban. Technical Report DOE/RL-96-51; PNNL-SA–27750, Pacific Northwest National Laboratory, PNNL, 1996.

[27] Martin B. Kalinowski, Anders Axelsson, Marc Bean, Xavier Blanchard, Theodore W. Bowyer, Guy Brachet, Simon Hebel, Justin I. McIntyre, Jana Peters, Christoph Pistner, Maria Raith, Anders Ringbom, Paul R. J. Saey, Clemens Schlosser, Trevor J. Stocki, Thomas Taffary, and R. Kurt Ungar. Discrimination of nuclear explosions against civilian sources based on atmospheric xenon isotopic activity ratios. *Pure and Applied Gephysics*, 167:517–539, 2010.

[28] P. R. J. Saey, M. Bean, A. Becker, J. Coyne, R. d' Armours, L.-E. De Geer, R. Hogue, T. J. Stocki, R. K. Ungar, and G. Wotawa. A long distance measurement of radioxenon in Yellowknife, Canada, in late october 2006. *Geophysical Research Letters*, 34:L20802, 2007.

[29] www.saunasystems.se/.

[30] A. Ringbom, K. Elmgren, K. Lindh, J. Peterson, T. W. Bowyer, J. C. Hayes, J. I. McIntyre, M. Panisko, and R. Williams. Measurements of radioxenon in ground level air in South Korea following the claimed nuclear test in North Korea. *Journal of Radioanalytical Chemistry*, 282:773–779, 2009.

[31] Glenn F. Knoll. *Radiation Detection and Measurement*. John Wiley & Sons, third edition, 2000.

[32] Shiego Shionoya and William M. Yen. *Phosphor Handbook*. CRC Press LCC, 1998.

[33] J. B. Birks. *The Theory and Practice of Scintillation Counting*. Pergamon Press Ltd., first edition, 1964.

[34] Matthias Auer, Timo Kumberg, Harmut Sartorius, Bernd Wernsberger, and Clemens Schlosser. Ten years of development of equipment for measurement of atmospheric radioactive xenon for the verification of the CTBT. *Pure and Applied Geophysics*, 167:471–486, 2010.

[35] J. I. McIntyre, K. H. Abel, T. W. Bowyer, J. C. Hayes, T. R. Heimbigner, M. E. Panisko, P. L. Reeder, and R. C. Thompson. Measurements of ambient radioxenon levels using the automated radioxenon sampler/analyzer (ARSA). *Journal of Radioanalytical and Nuclear Chemistry*, 248(3):629–635, 2001.

[36] Lloyd A. Currie. Limits for qualitative detection and quantitative determination. *Analytical Chemistry*, 40:586, 1968.

[37] http://www.detectors.saint-gobain.com/uploadedfiles/sgdetectors/documents/ product_data_sheets/bc400-404-408-412-416-data-sheet.pdf.

[38] Hood Chatham. Oxygen diffusion barrier properties of transport oxide coatings on polymeric substrates. *Surface and Coatings Technology*, 78:1–9, 1994.

[39] M. D. Groner, S. M. George, R. S. McLean, and P. F. Garcia. Gas diffusion barriers on polymers using Al_2O_3 atomic layer deposition. *Applied Physics Letters*, 88:051907, 2006.

[40] Riika L. Puurunen. Surface chemistry of atomic layer deposition: A case study for the trimethylaluminum/water process. *Journal of Applied Physics*, 97, 2005.

[41] M. D. Groner, F. H. Fabreguette, J. W. Elam, and S. M. George. Low-temperature Al_2O_3 atomic layer deposition. *Chemistry of Materials*, 16:639–645, 2004.

[42] John L. Vossen and Werner Kern, editors. *Thin Film Processes II*. Elsevier, 1991.

[43] Alexander Fay. Mitigation of the radioxenon memory effect in beta-gamma detector systems by deposition of thin film diffusion barriers on plastic scintillator. Master's thesis, University of Texas at Austin, 2010.

[44] H. Sjöstrand, E. Andersson Sunden, A. Conroy, G. Ericsson, M. Gatu Johnsson, L. Giacomelli, G. Gorini, C. Hellesen, A. Hjalmarsson, S. Popovichev, E. Ronchi, M. Tardocchi, M. Weiszflog, and JET EFDA Contributors. Gain stabilization control system of the upgraded magnetic proton recoil neutron spectrometer at JET. *Review of Scientific Instruments*, 80:063505, 2009.

[45] C. Moisan, F. Cayouet, and G. McDonald. *DETECT2000 The Object Oriented C++ Language Version of DETECT A Program for Modeling Optical Properties of Scintillators*.

[46] X-5 Monte Carlo Team. *MCNP - A General Monte Carlo N-Particle Transport Code, Version 5*, 2003.

[47] P. Mortreau and R. Berndt. Handbook of gamma spectrometry methods for non-destructive assay of nuclear materials. Technical Report EUR 19822 EN, Joint Research Centre, Ispra, Italy, 2010.